Laboratoire Aimé Cotton

Manipulation of Hydrogen Beam for the Detection of Gravitational Quantum States (GQS) with H

Ismat Abou Khechfe
M2 QLMN — Quantum, Light, Materials and Nanosciences

Supervisor: Daniel Comparat
Duration: March–August 2025

Acknowledgments

First and foremost, I am deeply grateful to my supervisor, Prof. Daniel Comparat, for his guidance from the very beginning of the internship and throughout. I am likewise grateful to all members of the MFC group at Laboratoire Aimé Cotton.

I would like to thank Dr. Hans Lignier for introducing me to LabVIEW, and the LAC Tech team—Henri Pezard, Bruno Vivan, and Christophe Siour—for their help in designing the heat shields. I am especially grateful to Dr. Martin Simon, who traveled from Vienna to explain me in detail the experimental setup.

My sincere thanks go to Pauline Yzombard, François Nez, and Pierre Bataille from the LKB group “Métrologie des systèmes simples et tests fondamentaux,” who introduced me to gravitational quantum states; our collaboration and regular meetings guided the evolution of the results. I also thank my friend and colleague in the Master’s program, Anthony El Bekaii, for reading this report and providing valuable comments.

Finally, I am grateful to Prof. Olivier Dulieu, Director of Laboratoire Aimé Cotton, for his help with administrative matters and, above all, for his moral support during my search for a PhD position.

Contents

Chapter 1

Introduction

1.1 Motivation

Gravitational Quantum States (GQS) arise when slow particles are confined between the Earth's gravitational potential and a reflective surface that produces quantum reflection. They were first observed with ultra-cold neutrons in 2002 [1], establishing quantised vertical motion over a mirror. Yet, despite decades of theoretical predictions, no atom has ever been seen in such states. Hydrogen (H) is an ideal candidate: its simple two-body nature permits high-precision calculations, and cryogenic sources can deliver orders-of-magnitude higher fluxes than neutron beams. Observing atomic GQS would therefore open a new window on short-range forces, tests of the weak equivalence principle in the quantum regime, and precision surface-potential metrology.

1.2 Quantum Gravitational States (GQS)

1.2.1 State of the art

The very first experimental evidence for gravitational quantum states arose in 2002, when ultra-cold neutrons were shown to occupy discrete vertical levels above a mirror [1] .

As we shall see, the spectra for neutrons (n), hydrogen (H) and antihydrogen ($\bar{\mathrm{H}}$) are practically identical. Whenever sufficiently slow particles feel the Earth's gravitational pull on one side and a repulsive mirror on the other, they become trapped in a triangular quantum well (Fig. 1.1). The derivation below starts with a neutral particle of atomic mass m; replacing m by the neutron or (anti)hydrogen mass leaves the analysis unchanged.

1.2.2 Triangular potential and governing equation

A particle in the gravitational field above an ideal horizontal mirror experiences

$$V(z) = mg\,z, \qquad z > 0, \tag{1.1}$$

with $g \simeq 9.81\ \mathrm{m\,s^{-2}}$. The vertical dynamics obey the time-independent Schrödinger equation

$$-\frac{\hbar^2}{2m}\,\frac{d^2\psi(z)}{dz^2} \;+\; mg\,z\,\psi(z) \;=\; E\,\psi(z), \tag{1.2}$$

supplemented by the boundary condition $\psi(0) = 0$.

Justification of the hard-wall boundary: Energies in the lowest quantum states are of order 10^{-12} eV—five orders of magnitude below the potential of a polished gold surface ($\sim 10^{-7}$ eV). Likewise, the surface potential increases over 10^{-9} m, whereas the de Broglie wavelength of the particle in a low GQS is 10 µm [2]. Hence the mirror appears as an *infinitely steep* barrier on the scale of the wave-packet, validating $\psi(0) = 0$.

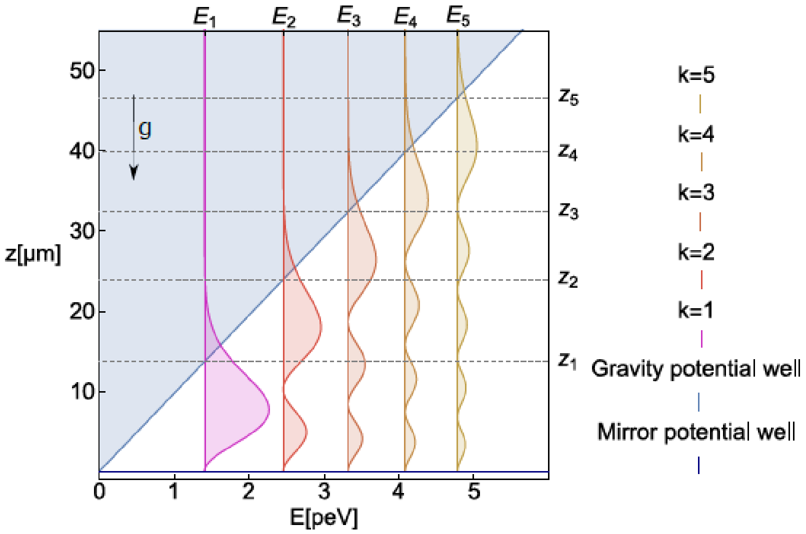

Figure 1.1: Gravitational potential and mirror barrier, together with the squared eigenfunctions $|\psi_n(z)|^2$ of the first five GQS [2].

1.2.3 Exact Airy-function solution

Equation (1.2) reduces to the Airy differential equation by introducing the characteristic length

$$z_0 = \left(\hbar^2/2m^2 g\right)^{1/3} = 5.87 \ \mu\text{m}.$$

Its solutions read

$$\psi_n(z) = C_n \ \text{Ai}(\xi_n), \qquad \xi_n = \frac{z}{z_0} - \lambda_n, \qquad E_n = mg\, z_0\, \lambda_n, \tag{1.3}$$

where λ_n denotes the n-th zero of $\text{Ai}(-\lambda)$, $(\psi(0) = 0)$. For the four lowest states

$$\lambda_{1..4} = 2.34,\ 4.09,\ 5.52,\ 6.79.$$

Associated energy, length and frequency scales follow:

$$\varepsilon_0 = mgz_0 = 0.602 \ \text{peV}, \qquad f_0 = \varepsilon_0/2\pi\hbar = 145 \ \text{Hz}.$$

1.2.4 Semiclassical approximation

To obtain an approximate description of the quantized energy levels E_n^{QS} for a particle (such as a neutron or H) bouncing vertically above a hard mirror in a gravitational potential, we can adopt a semiclassical approach based on the WKB [3].

According to the Bohr-Sommerfeld quantization rule, the energy levels in the gravitational quantum states (GQS) are approximately given by

$$E_n^{QS} = \sqrt[3]{\frac{9m}{8}\left(\pi\hbar g\left(n - \frac{1}{4}\right)\right)^2}, \qquad (n = 1, 2, 3, \dots). \tag{1.4}$$

As the quantum number n increases, the energy scales as $E_n^{\mathrm{QS}} \sim n^{2/3}$, and the spacing between consecutive levels decreases as $\Delta E_{n+1,n}^{\mathrm{QS}} \sim n^{-1/3}$. At high n, the energy levels become increasingly dense and gradually form a quasi-continuum.

Each energy level E_n corresponds to a classical turning point $z_n = E_n/(mg)$, i.e., the maximum height a classical particle with energy E_n would reach in the gravitational field. In quantum mechanics, the probability of finding the particle at height z is given by the squared modulus of the wave function, $|\psi_n(z)|^2$ (Fig. 1.1).

In the quantum description, although the wave function is mostly localized below the turning point z_n, it exhibits an exponentially decaying tail for $z > z_n$. The asymptotic form of this decay is given by:

$$\psi_n(\xi_n(z)) \to C_n\, \xi_n^{-1/4} \exp\left(-\frac{2}{3}\xi_n^{3/2}\right), \quad \text{for } \xi_n \to \infty \text{ (i.e. } z \to \infty). \tag{1.5}$$

The classical turning heights corresponding to the first four quantum states are approximately:

$$z_n = \{13.7,\ 24.0,\ 32.4,\ 39.9\}\,\mu\mathrm{m}. \tag{1.6}$$

For a clearer and more pedagogical explanation of gravitational quantum states (GQS) and the WKB approximation in this context, see [3], Section 2.5, pp. 110–116.

Using the known eigenfunctions, we can derive their Fourier transform, and then obtain the amplitudes $\phi_n(v)$ measuring the velocity distribution of the particle in the n^{th} quantum state:

$$\phi_n(v) = \sqrt{\frac{m}{2\pi\hbar}} \int_0^\infty \psi_n(z)\, e^{-imvz/\hbar}\, dz. \tag{1.7}$$

From Eq. (1.3) the natural gravitational scales are:

$$z_0 = \left(\frac{\hbar^2}{2m^2 g}\right)^{1/3}, \qquad \varepsilon_0 = mgz_0, \tag{1.8}$$

and the corresponding velocity

$$v_0 = \sqrt{\frac{2\varepsilon_0}{m}} = \sqrt{2gz_0} \approx 1.07\ \mathrm{cm\,s^{-1}} \quad \text{(for neutrons)}. \tag{1.9}$$

We set dimensionless variables $\eta := z/z_0$ and $u := v/v_0$. Since $mv_0z_0/\hbar = 1$, the amplitudes $\phi_n(v)$ become:

$$\phi_n(v_0 u) = \sqrt{\frac{m}{2\pi\hbar}}\, z_0 \int_0^\infty \psi_n(z_0\eta)\, e^{-iu\eta}\, d\eta. \tag{1.10}$$

Thus v_0 sets the natural scale (i.e., the width) of the vertical velocity distribution $|\phi_n(v)|^2$.

1.2.5 Why neutrons, hydrogen and antihydrogen behave alike

At this point, it becomes clear why gravitational quantum states (GQS) for different particles such as neutrons, hydrogen, or antihydrogen are expected to emerge through essentially the same physical mechanism.

The key reason is that the only parameter entering the Schrödinger equation for a neutral particle above an ideal mirror is the particle's mass. Since the masses of neutrons, hydrogen, and antihydrogen are all very close to the atomic mass unit, they experience nearly identical dynamics under gravity in the presence of a reflective surface which acts almost like a perfect mirror.

1.3 Historical Observation of Gravitational Quantum States (GQS)

The first direct observation of gravitational quantum states (GQS) was performed using ultracold neutrons (UCN). In these experiments, a neutron beam was directed above a horizontal mirror, with an absorber placed at a variable height Δl above it, creating a slit through which neutrons could pass. The number of neutrons transmitted through this slit was measured as a function of Δl, revealing signatures of quantized motion in the gravitational field.

Because of the intrinsic properties of gravitational quantum states (GQS), some technical barriers must be overcome to observe them with atoms. In order to form observable GQS, particles must remain confined long enough between the gravitational potential and the reflecting surface. According to the Heisenberg uncertainty principle $\Delta t\,\Delta E \gtrsim \hbar/2$, the time of flight Δt spent by the atoms in the confinement region must be long enough that the energy uncertainty ΔE becomes much smaller than the typical energy scale of GQS, on the order of pico-electronvolts (peV).

This condition determines the required horizontal velocity of the particles and the corresponding length of the mirror and absorber system, as illustrated in Fig. 1.2.

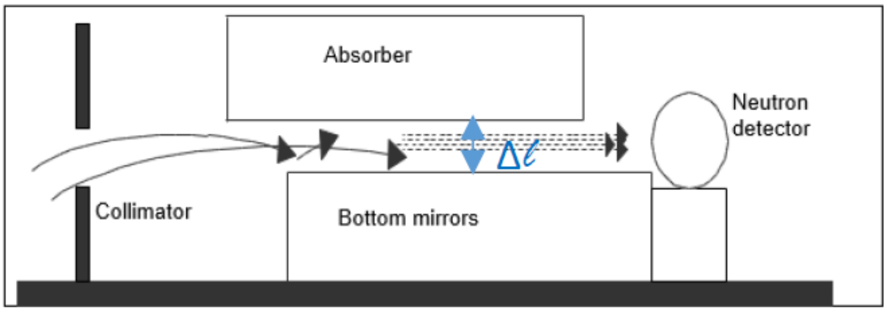

Figure 1.2: Schematic of the historical experiment [1].

In the vertical direction, quantum states emerge due to the confinement of neutrons between the mirror and the gravitational potential. These eigenenergies are given by $E_n = mgz_0\lambda_n$, where λ_n are the zeros of the Airy function and $mgz_0 = 0.602\,\text{peV}$. For instance, the first two levels have energies $E_1 \approx 1.41\,\text{peV}$ and $E_2 \approx 2.46\,\text{peV}$, with an energy separation of approximately $1.05\,\text{peV}$. To resolve these levels experimentally, the uncertainty in the vertical energy ΔE must be smaller than this gap. Since $\Delta E \sim mg\Delta z$, this imposes a constraint on the vertical confinement length $\Delta z < 10\,\mu\text{m}$. By the Heisenberg relation, this implies an uncertainty in vertical velocity $\Delta v_z \sim \hbar/(2m\Delta z)$, which is on the order of $0.3\,\mathrm{cm/s}$. This is consistent with the characteristic vertical velocity of the first quantum state, $v_z \sim 1.07\,\mathrm{cm/s}$, confirming that very narrow vertical collimation is essential to observe GQS. This justifies the use of an upstream collimator to limit the vertical divergence of the neutron beam.

The slit height Δl between the horizontal mirror and the absorber determines which vertical quantum states can pass through. When Δl is much larger than the classical turning point z_n of a given state, neutrons in that state pass with minimal loss. As Δl decreases, the neutron wavefunction $\psi_n(z)$ begins to overlap with the absorber, leading to increased absorption and a drop in transmission. When Δl becomes smaller than z_n, neutrons in the n-th state are mostly absorbed and cannot be transmitted.

This behavior leads to a characteristic step-wise signal in the detected neutron flux. For $\Delta l < z_1$, no gravitational quantum state can exist between the mirror and the absorber, so the transmitted flux is essentially zero. As soon as $\Delta l = z_1$, the first quantum state fits into the slit, and a sudden increase in the detected flux occurs. The flux then stays approximately constant until $\Delta l = z_2$, where the second state begins to contribute. This results in another step, and so on for higher states. This discrete, step-by-step appearance of the flux is a direct signature of gravitational quantum states and clearly differs from the smooth classical expectation.

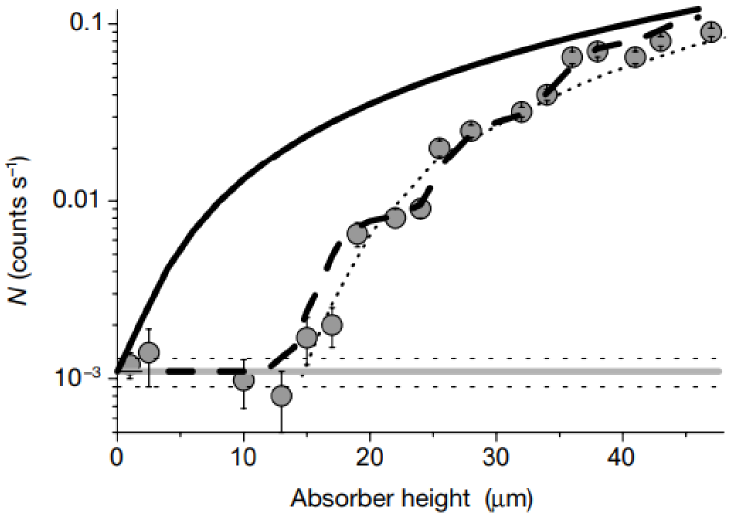

Figure 1.3: Neutron transmission as a function of slit height Δl showing step-wise increases, characteristic of quantum gravitational bound states. Black points: measured transmission. Solid curve: classical expectation $N \propto (\Delta l)^{3/2}$. The dashed curve is a quantum-mechanical fit: in which all level populations and the height resolution are fitted from the experimental data. The dotted curve is a truncated fit that assumes only the lowest quantum state contributes below its turning height, producing the first step. [1].

The differences between the experiment performed with neutrons and the one we will perform with hydrogen lie in the distinct methods used to produce and detect the particles, and since we have different lengths of the mirror-absorber system, in their different longitudinal velocities. Additionally, the mechanisms by which the particles interact with the scatterer differ between the two cases.

Chapter 2

Manipulation of the Hydrogen Beam I

2.1 Our experimental setup

In our lab, an existing apparatus, used for spectroscopic measurements, is available that we need to modify to perform the detection of (GQS).

Our experiment is designed to detect gravitational quantum states (GQS) using a beam of atomic hydrogen (H). The hydrogen atoms are produced from an ultrapure water (H_2O) source. First, ultrapure H_2O undergoes electrolysis to produce molecular hydrogen (H_2). The resulting H_2 gas is then injected into a microwave (MW) discharge cavity, where a plasma is sustained to dissociate H_2 molecules into atomic hydrogen (H).

The atomic hydrogen beam is cooled in a cryogenic environment then one Zeeman deceleration pulsed coil will be employed to reduce and control the longitudinal velocity v_z, using magnetic field gradients acting on the magnetic moment of the atoms. After deceleration, a magnetic hexapole will be used to focus and collimate the beam in the transverse directions (x and y) by exploiting the state-dependent magnetic potential [5].

The detection system consists of an absorber–mirror assembly, with the mirror providing vertical confinement in the gravitational field (g). Atoms exiting this region are detected at the end of the setup.

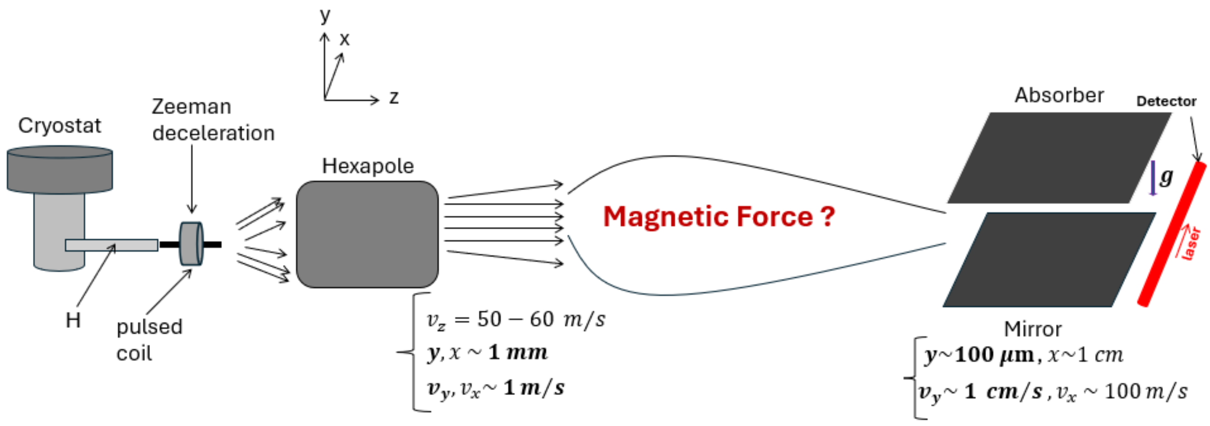

Figure 2.1: Simplified schematic of our setup. Hydrogen atoms are cooled in a cryostat, decelerated by a pulsed Zeeman coil, focused by a magnetic hexapole, and guided into a gravitational quantum state detection region composed of an absorber–mirror assembly and then detected with a pulsed laser.

2.1.1 Velocity selection and target range for GQS detection

In our experiment, the atomic hydrogen beam is cooled to approximately 6 K, and we cannot lower it further; otherwise, the atoms freeze out onto the cryostat walls. At the exit of the cryostat through a small aperture, the velocity distribution of the atoms follows the well-known effusive Maxwell–Boltzmann distribution. This initial velocity profile is illustrated in Fig. 2.2.

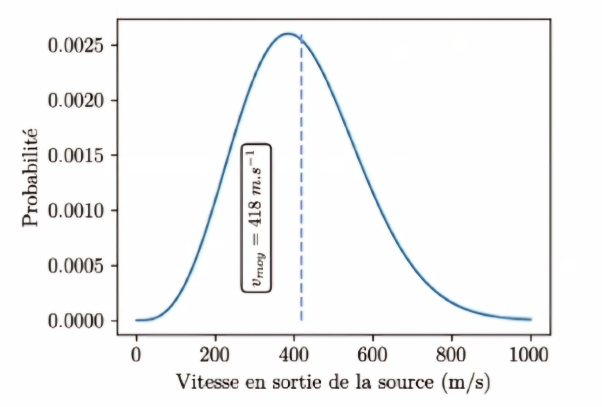

Figure 2.2: Effusive Maxwell–Boltzmann distribution of the atomic hydrogen beam at the exit of the cryostat at $T \approx 6$ K.

According to scaling arguments based on the 2002 neutron gravitational quantum state experiment by Nesvizhevsky *et al.* Ref. [1], for a mirror length of 30 cm the optimal conditions for observing the first gravitational quantum states with hydrogen atoms require time of flight of about 0.5 ms. These parameters imply that the longitudinal velocity of the atomic beam should be 50 m/s.

In principle, one could aim to decelerate atoms located near the peak of the initial velocity distribution in order to maximise the number of atoms in the target velocity range. However, reducing the speed from the distribution maximum down to 50–60 m/s would require a magnetic force far greater than what is experimentally feasible with our electronics and coil design.

For this reason, we instead choose to isolate a narrower fraction of the distribution—atoms with velocities between 190 and 210 m/s (highlighted in green in Fig. 2.3)—and then decelerate only this portion to the desired 50–60 m/s range. This approach reduces the required magnetic force to a practical level. Numerical simulations carried out by Pierre Bataille (post-doctoral researcher at LKB) confirm that such a velocity reduction can be achieved using one pulsed Zeeman decelerator coil.

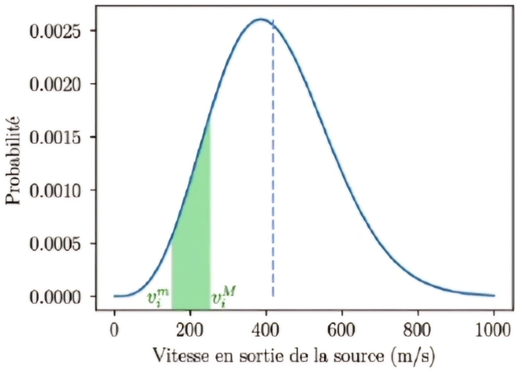

Figure 2.3: Selected portion of the effusive velocity distribution (green) between 190 and 210 m/s to be decelerated down to 50–60 m/s.

2.1.2 Principle of Zeeman deceleration

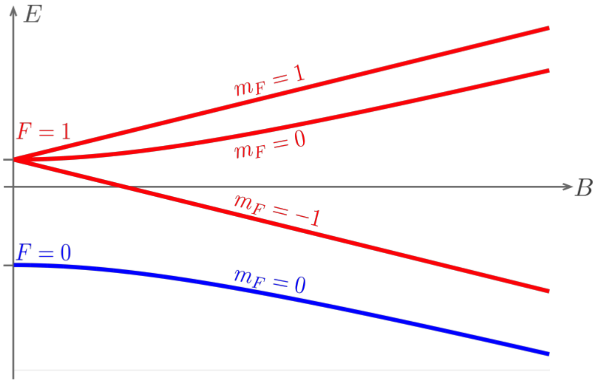

Figure 2.4: Zeeman energy levels for the hydrogen ground state.

In all our study, we work with the $|F = 1, m_F = 1\rangle$ state. Following the conventions of Jansen and Merkt [5], the first–order Zeeman shift of a hyperfine state $|F = 1, m_F = 1\rangle$ reads

$$U_{\text{mag}}(z) = g_F\, m_F\, \mu_B\, B(z), \tag{2.1}$$

where g_F is the hyperfine Landé factor, m_F the magnetic quantum number and μ_B the Bohr magneton. The corresponding effective magnetic dipole moment is

$$\mu_{\text{eff}} = -\frac{\partial U_{\text{mag}}}{\partial|\mathbf{B}|} = -\, g_F\, m_F\, \mu_B, \tag{2.2}$$

so that the longitudinal force in an inhomogeneous field becomes

$$F_z = \mu_{\text{eff}} \frac{\partial B(z)}{\partial z} = -\, g_F\, m_F\, \mu_B \frac{\partial B(z)}{\partial z}. \tag{2.3}$$

If $g_F m_F > 0$ (“low-field-seeking”) and the field increases $\big(\partial B/\partial z > 0\big)$, Eq. (2.3) gives $F_z < 0$: the atom is decelerated and the kinetic energy is converted into magnetic potential energy. For $g_F m_F < 0$ (“high-field-seeking”) the force is in the same direction as the gradient and the atom is accelerated, while states with $m_F = 0$ experience only second-order forces. Hence, in ground-state hydrogen the sublevel $|F = 1, m_F = 1\rangle$ is the only component slowed in a Zeeman decelerator, providing intrinsic state selectivity.

Fig. 2.5. A net velocity reduction is obtained by switching off the magnetic field precisely when the atom reaches the maximum of the potential barrier, so that none of the stored magnetic energy is reconverted into kinetic energy on the downstream side. Fast current pulses in the deceleration coil accomplish this timing.

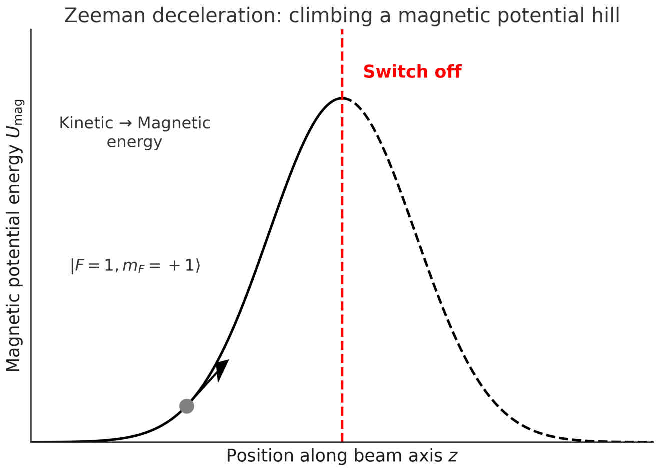

Figure 2.5: Schematic illustration of Zeeman deceleration: an atom climbs the magnetic potential barrier and the field is switched off at the maximum, preventing re-acceleration.

2.1.3 Magnetic hexapole refocusing

Immediately downstream of the pulsed coil the hydrogen packet acquires a sizeable transverse spread: atoms that have lost longitudinal speed diverge radially. A static magnetic hexapole provides the required refocusing, because its field grows quadratically with radius and exerts a restoring force on the low-field-seeking sublevel $|F = 1, m_F = 1\rangle$; high-field-seekers are defocused and leave the beam. The simulation of the hexapole stage for our geometry remains to be carried out.

2.2 Manipulating the beam to fulfil GQS detection requirements

2.2.1 Transverse requirements along the gravitational axis

In chapter 1 we showed that the vertical coordinate y (parallel to g) must remain within the characteristic length scale of the lowest gravitational quantum states, and that the corresponding vertical velocity should be of order $v_y \sim 1$ cm/s. Figure 2.1 (page 9) sketches the profil of the beam after the hexapole: the packet typically emerges with

$$y, x \simeq 1 \text{ mm}, \qquad v_y, v_x \simeq 1 \text{ m/s}, \qquad v_z = 50-60 \text{ m/s}.$$

To meet the GQS detection conditions we therefore have to compress y by one order of magnitude, down to $y \approx 100$ µm, and reduce the vertical velocity spread at the same time to $v_y \approx 1$ cm/s, while leaving the longitudinal velocity v_z unchanged because it already lies in the required range.

2.2.2 Liouville's theorem in phase space

Consider a Hamiltonian system with canonical coordinates (q, p) and Hamiltonian $\mathcal{H}(q, p)$. Each point $\boldsymbol{\zeta} = (q, p)$ moves with velocity

$$\dot{\boldsymbol{\zeta}} = (\dot{q}, \dot{p}) = \left(\frac{\partial \mathcal{H}}{\partial p}, -\frac{\partial \mathcal{H}}{\partial q}\right), \tag{2.4}$$

so the phase–space divergence is

$$\begin{aligned}\nabla \cdot \dot{\boldsymbol{\zeta}} &= \frac{\partial \dot{q}}{\partial q} + \frac{\partial \dot{p}}{\partial p} \\ &= \frac{\partial}{\partial q}\left(\frac{\partial \mathcal{H}}{\partial p}\right) + \frac{\partial}{\partial p}\left(-\frac{\partial \mathcal{H}}{\partial q}\right) = 0. \end{aligned} \tag{2.5}$$

because mixed partial derivatives commute. Hence the volume (area) enclosed by any material surface that moves with the phase points is constant in time; the phase–space density is incompressible. This result, proven for one degree of freedom and easily generalised to $2n$ dimensions, is Liouville's theorem (Taylor, *Classical Mechanics*, Sec. 13.6)-[6]. Liouville's theorem remains valid even when $\mathcal{H}(q, p, t)$ depends explicitly on time. For a three–dimensional N-particle system the state corresponds to a point in a $6N$-dimensional phase space or, equivalently, to N points in a six-dimensional space; when N is very large these points form an incompressible "fluid" in the continuous limit whose density $\rho = N/V$ satisfies $\mathrm{d}\rho/\mathrm{d}t = 0$ (also constant).

2.2.3 Compressing the (y, v_y) subspace

In other experimental schemes, a set of mechanical slits is used to limit the transverse extent, but this inevitably discards a large fraction of the beam. The first-order Stark effect for ground-state hydrogen vanishes. Dissipative forces are also not feasible for this state: Doppler laser cooling would require ultraviolet wavelengths that are presently impractical. For these reasons, our strategy has been to identify a magnetic field configuration—equivalently, a conservative force field—that can achieve the desired compression in (y, v_y) while compensating in (x, v_x). From Liouville's theorem we know that the volume in 6D phase space is conserved under Hamiltonian evolution. Our initial approach was therefore to search for a conservative magnetic force that could reduce the phase–space area in the subspace (y, v_y), while producing a compensating increase in another canonical pair, here (x, v_x), since the x direction is not constrained (mirror width of ~ 10 cm) and v_z should be unchanged since it is already in the required range. So we work in $4D$ phase space (x, v_x, y, v_y), where the volume is again conserved because we decoupled from z.

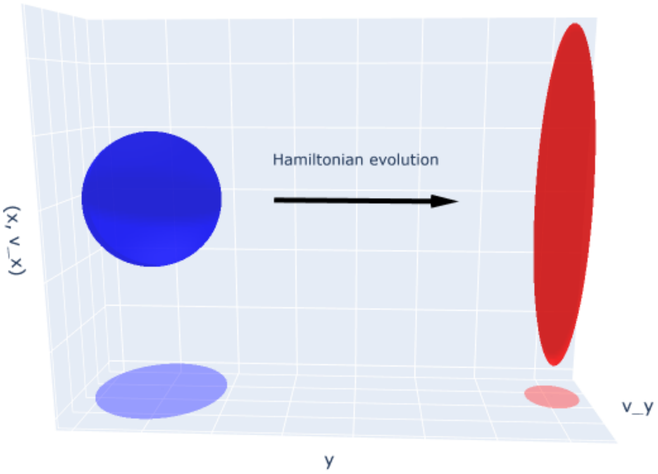

Figure 2.6: Our idea was to find a Hamiltonian evolution that shears the initial volume in the 4D space (x, v_x, y, v_y) along the (x, v_x) direction, so that the projection area onto the (y, v_y) plane decreases while maintaining the total volume constant. The figure also shows, the projection onto the (y, v_y) plane. We will examine in the following whether this is possible or not.

How do we approach the problem?

- Track individual particle trajectories in the phase space (x, v_x, y, v_y) under the action of a conservative force:

$$\vec{F} = -\nabla V(x, y) \tag{2.6}$$

$$\vec{F} = -\nabla \left(E(F, m_F)\right) \tag{2.7}$$

$$\vec{F} = -\nabla \left(\mu \|\vec{B}\|\right) \qquad \text{for the state } |F = 1,\, m_F = 1\rangle \tag{2.8}$$

- Compute the area of the convex hull (i.e., the maximum area in phase space):
  - A decrease in convex hull area implies a decrease in the area in the (y, v_y) subspace.

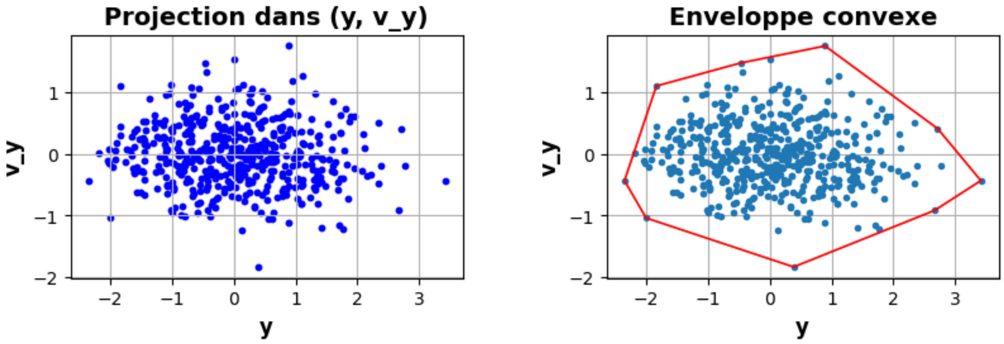

Figure 2.7: Left: projection in (y, v_y). Right: corresponding convex hull. Random Gaussian distribution in phase space just to show the concept of convex hull.

A force from two wires with opposite currents

We first considered a configuration of two parallel wires aligned along the z-axis, positioned symmetrically at opposite y-coordinates and carrying opposite currents. This served as a first simple example: we considered the resulting magnetic field, the corresponding force exerted on the atoms, and the evolution of an initial Gaussian distribution in order to gain intuition into the dynamics in phase space.

In Fig. 2.8 (left) we show the resultant magnetic field in the (x, y) plane, and in Fig. 2.8 (right) the corresponding magnetic force field. A series expansion of the force around the origin gives

$$F_x \approx k\,x, \qquad F_y \approx -k\,y, \tag{2.9}$$

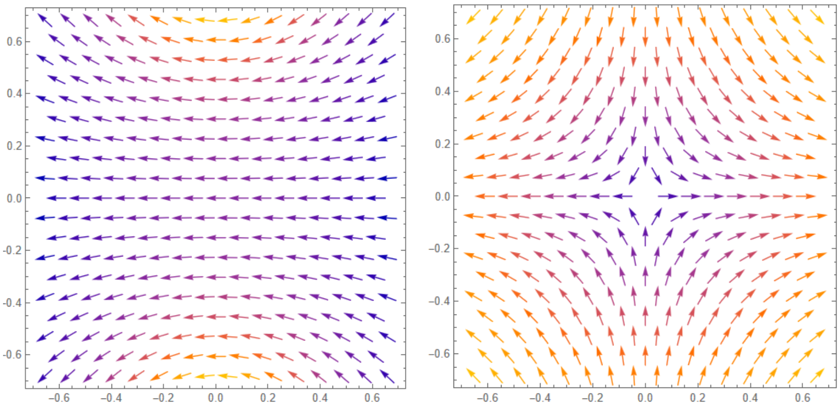

Figure 2.8: Magnetic field (left) and corresponding force field (right) in the (x, y) plane for two parallel wires along z with opposite currents placed at $(0,\ d)$ and $(0,\ -d)$ where $d = 1m$ here. Where x axis is the horizontal axis here and the color code is the by-default *Mathematica* code: Modulus ascending from blue to red.

We studied the evolution of initial ellipses in phase space with the linearized forces, and understood the underlying physics using transfer matrices. The motion in (y, v_y) is harmonic, corresponding to a rotation in phase space, while the motion in (x, v_x) is hyperbolic, leading to an elongation of the ellipse. In both subspaces, however, the area is conserve because x and y are decoupled, so Liouville's theorem applies separately to each subspace.

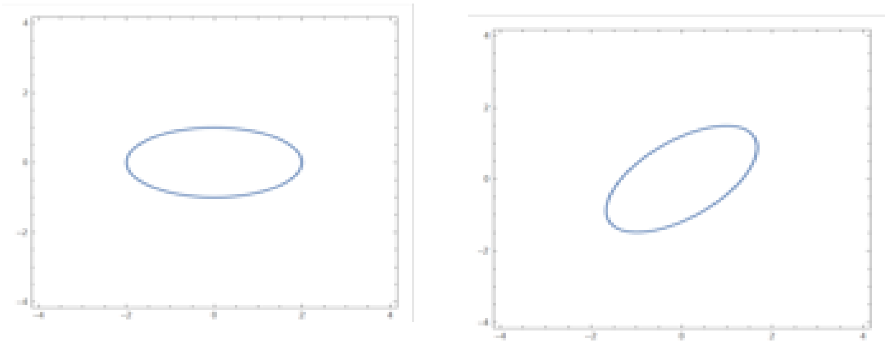

Figure 2.9: Evolution of an initial ellipse in the (y, v_y) phase space under harmonic motion: the area is conserved, the ellipse is rotated.

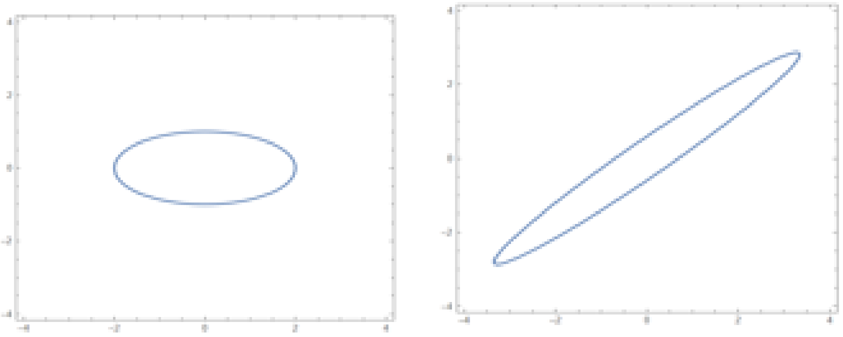

Figure 2.10: Evolution of an initial ellipse in the (x, v_x) phase space under hyperbolic motion: the area is conserved, the ellipse is elongated.

A General Linear Force

I considered then a more general linear force of the form:

$$\begin{cases} F_y = ax + by \\ F_x = cx + dy \end{cases}$$

Numerical simulation with 16 random points

I took 16 random points in the 4D phase space and solved the equations of motion using *Mathematica*. I then followed the evolution in the (y, v_y) subspace and observed a clear alignment of the points and a significant decrease in the area of their convex hull for the chosen parameters $a = 0.01$, $d = 152000$, and $b = c = 0$. This behavior is illustrated in Figure 2.11.

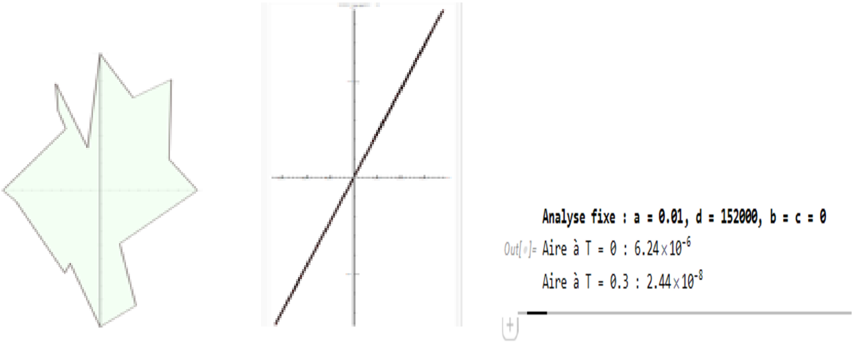

```
Analyse fixe : a = 0.01, d = 152000, b = c = 0
Out[ ]= Aire à T = 0 : 6.24×10^-6
        Aire à T = 0.3 : 2.44×10^-8
```

Figure 2.11: Left: Initial configuration of 16 random points in (y, v_y) subspace. Middle: Alignment after evolution. Right: Decrease of the convex hull area, where T represents the distance Z traveled by the particles.

Later, when returning to the magnetic field configuration, I realized that for the force to be conservative (derive from a potential), i.e., $\vec{F} = -\vec{\nabla} V$, since the curl of a gradient always vanishes, we should impose the condition $\vec{\nabla} \times \vec{F} = 0$, which leads to the constraint $a = d$. This ensures that the force is conservative. So, our result is not a conservative force.

Now I imposed the condition $a = d$, and for a technical reason that will be explained later, I initially took a symmetric distribution in phase space. Then, by manually scanning the remaining parameters, we never observed a decrease of the area of the convex hull. Even with an automatic code that searches for the minimum area of the convex hull over a wide range of parameter combinations, it never yields an area smaller than the initial one! At this point, I started thinking about a general proof that with a linear force, it is impossible to compress the (y, v_y) subspace.

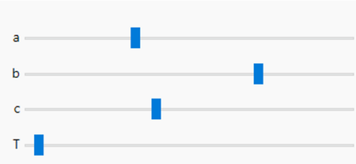

Figure 2.12: Manual parameter scanning with sliders.

A comment on the magnetic field case

You may say at this point that the magnetic field is more constrained because it must satisfy Maxwell's equations. But it is useless since if it does not work with a general linear force, it will not work by adding more constraints. Despite that, I include in Appendix A the full calculations I performed, starting from a linearized 3D magnetic field and imposing the static Maxwell conditions: $\nabla \cdot \vec{B} = 0$ and $\nabla \times \vec{B} = 0$. Then, I solved the equations of motion using *Mathematica*.

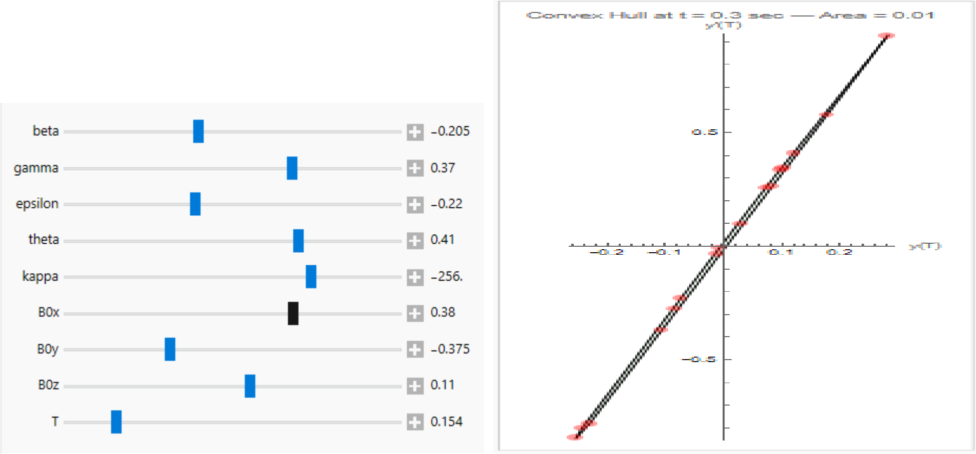

beta −0.205
gamma 0.37
epsilon −0.22
theta 0.41
kappa −256.
B0x 0.38
B0y −0.375
B0z 0.11
T 0.154

Figure 2.13: Sliders controlling the magnetic field parameters and here simulation time T.

Despite exploring many combinations of parameters with these sliders, I never observed any decrease in the area of the convex hull compared to the initial one in either the (x, v_x) or the (y, v_y) subspaces.

2.3 Gromov's Theorem Uncovered

After that, we began exploring nonlinear forces. I tested several cubic and fourth-order coupled potentials, but the result was always the same: the area of the projection in (y, v_y) was never smaller than the initial one. In most cases, it even increased.

While searching through the literature, I found the article [7]which explores the same idea and cites Gromov's non-squeezing theorem.

Beyond the conservation of phase-space volume, symplectic maps also obey a much stronger constraint known as Gromov's non-squeezing theorem. This celebrated result, proved in 1985, states that it is impossible to map a symplectic ball $B^{2n}(r)$ of radius r into a symplectic cylinder $Z_j^{2n}(R)$ of smaller radius $R < r$ via any symplectic transformation. Formally, if there exists a symplectic map φ such that

$$\varphi : B^{2n}(r) \longrightarrow Z_j^{2n}(R),$$

then necessarily $r \leq R$.

The ball and cylinder are defined as:

$$B^{2n}(r) \equiv \left\{ \left(x^1, x^2, \ldots, x^n, p_1, p_2, \ldots, p_n\right) \in \mathbb{R}^{2n} \,\middle|\, \sum_{i=1}^{n} (p_i^2 + x^{i2}) < r^2 \right\}, \tag{2.10}$$

$$Z_j^{2n}(R) \equiv \left\{ \left(x^1, x^2, \ldots, x^n, p_1, p_2, \ldots, p_n\right) \in \mathbb{R}^{2n} \,\middle|\, p_j^2 + x^{j2} < R^2 \right\}. \tag{2.11}$$

This result is often interpreted as a "symplectic rigidity" theorem: although the ball $B^{2n}(r)$ is fully contained in the cylinder $Z_j^{2n}(R)$ when $r = R$, no symplectic transformation can squeeze a larger ball $B^{2n}(R + \varepsilon)$ into the same cylinder.

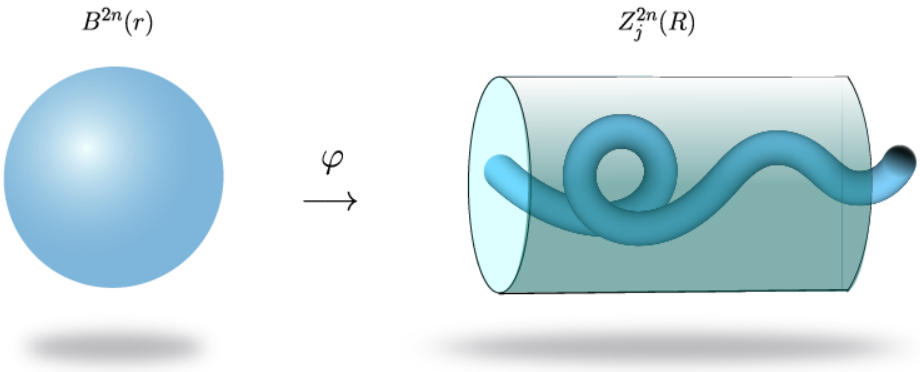

[7].

Figure. Gromov's non-squeezing theorem illustrated. No symplectic map φ can squeeze the ball $B^{2n}(r)$ into the cylinder $Z_j^{2n}(R)$ if $r > R$. However, for $r \leq R$, the ball already fits symplectically.

The link to our work An equivalent statement of Gromov's theorem is: "*No canonical transformation can squeeze a phase–space ball B_R through a circular hole of radius $r < R$ cut in a conjugate plane $\Pi_j \equiv \{x_j, p_j\}$*". Because Hamiltonian dynamics are canonical, this implies that in phase space (in our case $4D$ phase space), we cannot compress the distribution with Hamiltonian dynamics in such a way that the projection in a conjugate subplane (in our case, (y, v_y)) shrinks below its initial area.

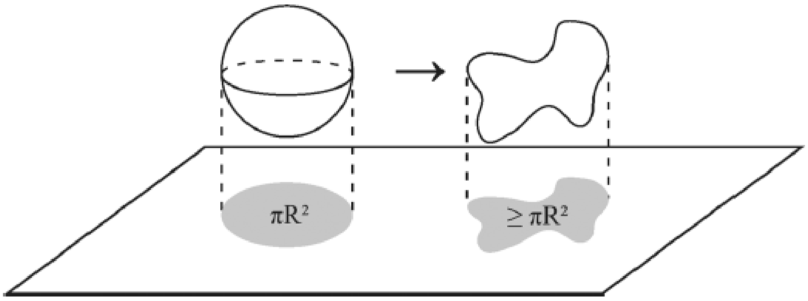

Figure 2.14: Shadow of a deformed ball under Hamiltonian evolution Ref. [8].

For a better understanding of symplectic geometry and Gromov's theorem see Appendix. D.

2.4 Conclusion.

We conclude that our idea of decreasing the area in the (y, v_y) plane while increasing it in the (x, v_x) plane is topologically forbidden. Although the idea may seem naive in hindsight, approaching the problem from the right perspective has brought valuable insights. In particular, it explains why our simulations consistently failed to compress the projection in (y, v_y). More importantly, this investigation led us to discover a theorem that, while not widely known, at least in our lab group, is significantly more powerful than Liouville's theorem. Unlike Liouville's, which only asserts volume preservation, this result imposes stricter constraints on how distributions can evolve in phase space, ruling out certain intuitive but incorrect strategies like the one we initially explored.

Chapter 3

Manipulation of the Hydrogen Beam II

3.1 Requirement for laser-based detection

After the pulsed coil shown in Fig. 2.1, previous simulations indicate that the hydrogen beam forms a $\sim 3\,\text{mm}$-long bunch with longitudinal velocities in the range 50–60 $\text{m}\,\text{s}^{-1}$. At the detection plane, we probe the beam with a 10 ns pulsed laser of 1 mm (see Fig. 3.4).

Since we use a 10 ns pulsed laser and the initial bunch has a velocity dispersion of about 10 m/s, a large fraction of atoms will be lost during the detection, which will in turn weaken the signal. So our objective is to engineer a magnetic-field profile—hence a longitudinal force—that produces temporal (time-of-flight) focusing at the detector: atoms originating from the initial bunch should arrive simultaneously within the 1 mm laser spot. Attending this condition increases the number of atoms within the laser volume per pulse and thus enhances the detected signal.

3.2 1D model: linear-force pulse

In order to gain an initial understanding of the problem, I began by simplifying it and studying a simple case. Therefore, I first considered the system only along the z-axis (1D), neglecting the initial spatial extent, and neglected the intial bunch length as if the atoms are emitted from the same point with longitudinal velocities uniformly spanning 50–60 $\text{m}\,\text{s}^{-1}$. I chose the detection plane randomly at $z = 5$ m. Our first idea was to test a linear longitudinal force

$$F(z) = k\,(z - z_c), \tag{3.1}$$

where z_c is the position of the bunch center at the activation time of the force. We apply this force as a short pulse so that atoms located before the center are accelerated and atoms located after the center are decelerated, leading to temporal focusing at the detector. The pulse must be short enough that atoms located before z_c do not cross to the other side during the activation; otherwise they would be re-decelerated.

In the first simulation we chose $z_c = 2.5$ m and obtained an effective slope

$$k \approx -1.47 \times 10^{-21}\ \text{N}\,\text{m}^{-1},$$

with a pulse duration of 50 μs (from $t_{\text{on}} = 45.430$ ms to $t_{\text{off}} = 45.480$ ms). This pulsed linear force reduces the arrival-time spread from 16.67 ms (no force) to 0.03 ms (Fig. 3.1).

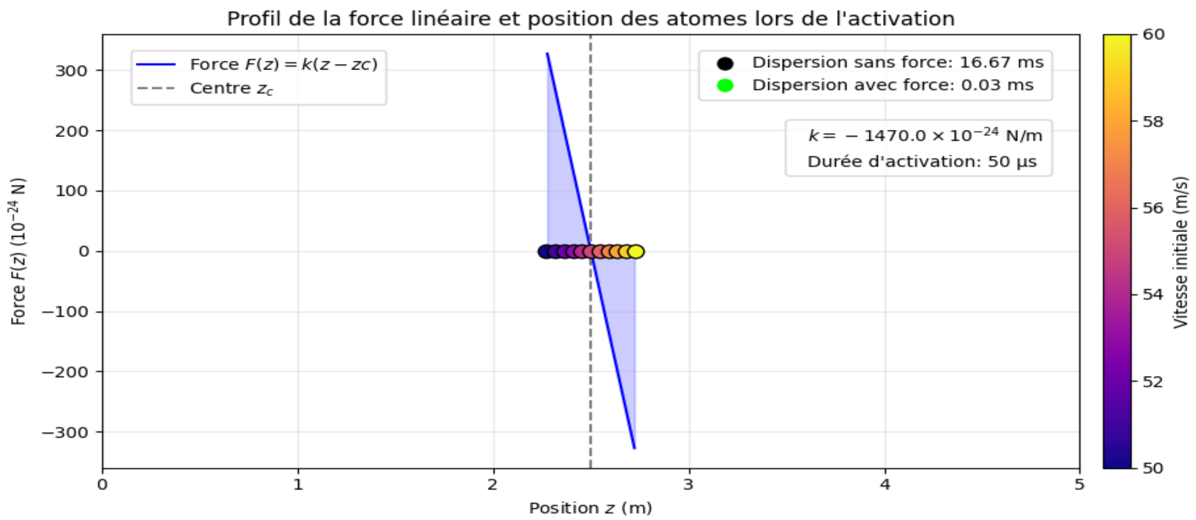

Figure 3.1: 1D linear-force pulse: parameters and achieved temporal focusing.

To illustrate the dynamics, Fig. 3.2 shows three frames of the simulation.

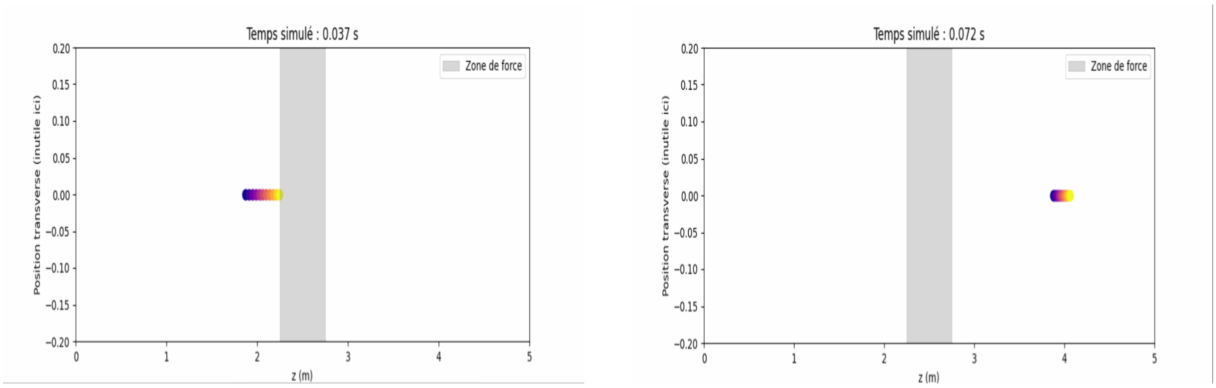

(a) $t \approx 0.037$ s: bunch approaching the force zone.

(b) $t \approx 0.072$ s: beam refocusing.

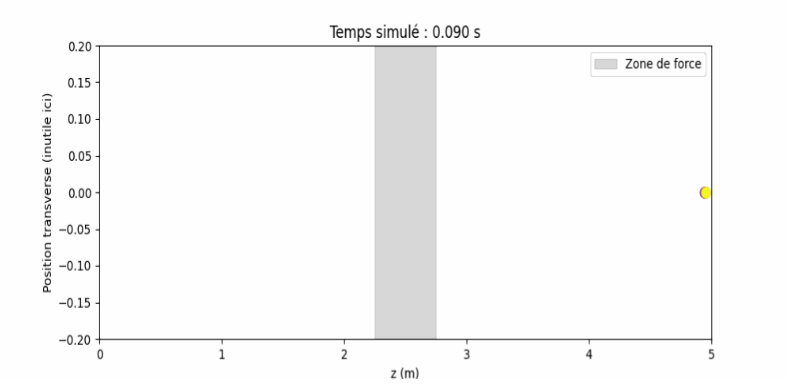

(c) $t \approx 0.090$ s: atoms before arriving together at $z = 5$ m.

Figure 3.2: Three frames from the 1D simulation showing temporal focusing with a pulsed linear force.

3.3 Real-coil magnetic force for $F = 1$, $m_F = 1$

We work throughout with the low-field–seeking hyperfine state $F = 1$, $m_F = 1$ of hydrogen, hence $g_F = 1$ and $m_F = 1$, see Chapter 2. In the linear Zeeman regime, the level shift is simply: (see [5])

$$W_Z(z) = \mu_B \, B(z), \tag{3.2}$$

so the axial force is minus the gradient,

$$F_z(z) = -\frac{dW_Z}{dz} = -\,\mu_B \, \frac{dB}{dz}. \tag{3.3}$$

For a thin circular coil of radius R with N turns and current I, centered at $z = z_b$, the on-axis field is

$$B(z) = \frac{\mu_0 N I R^2}{2\,[\,R^2 + (z - z_b)^2\,]^{3/2}}, \tag{3.4}$$

whose derivative is

$$\frac{dB}{dz} = -\frac{3\,\mu_0 N I R^2\,(z - z_b)}{2\,[\,R^2 + (z - z_b)^2\,]^{5/2}}. \tag{3.5}$$

Inserting (3.5) into (3.3) gives the on-axis magnetic force for our working state:

$$\boxed{F_z(z) = \frac{3\,\mu_B\,\mu_0\,N\,I\,R^2\,(z - z_b)}{2\,[\,R^2 + (z - z_b)^2\,]^{5/2}}}. \tag{3.6}$$

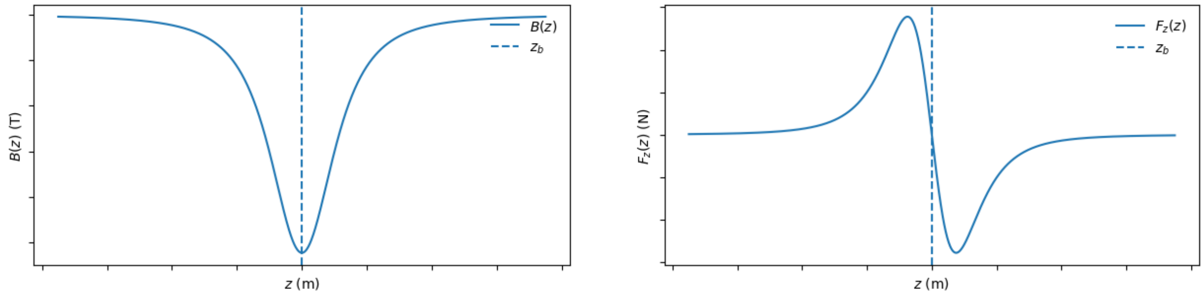

(a) On-axis magnetic field $B(z)$ from Eq. (3.4). The dashed line marks z_b.

(b) Axial force $F_z(z)$ for the working state F=1, m_F=1, obtained from Eq. (3.6) with a negative current.

Figure 3.3: On-axis field and force used in the simulations. Formulas correspond to Eqs. (3.4) and (3.6).

3.3.1 Linear expansion of the real-coil force

As shown in Sect. 3.2, a linear (pulsed) force might suffice to achieve temporal focusing. We now ask when the real-coil force (3.6) behaves linearly around its center and thus reproduces the same effect. For direct comparison we align the centers, $z_b = z_c$, and write $\delta z \equiv z - z_b$. For our working state $F = 1$, $m_F = 1$ the on-axis force is

$$F_z(z) = \frac{3\,\mu_B\,\mu_0\,N\,I\,R^2\,\delta z}{2\,[\,R^2 + (\delta z)^2\,]^{5/2}}. \tag{3.7}$$

Factorizing R and expanding for $|\delta z| \ll R$,

$$\begin{aligned} F_z(z) &= \frac{3\,\mu_B\,\mu_0\,N\,I}{2\,R^3}\,\delta z\left(1+\frac{(\delta z)^2}{R^2}\right)^{-5/2} \\ &= \frac{3\,\mu_B\,\mu_0\,N\,I}{2\,R^3}\,\delta z\left[1-\frac{5}{2}\frac{(\delta z)^2}{R^2}+\frac{35}{8}\frac{(\delta z)^4}{R^4}+\mathcal{O}\!\left(\frac{(\delta z)^6}{R^6}\right)\right]. \end{aligned} \tag{3.8}$$

To first order,

$$\boxed{F_z(z) \simeq k\,\delta z, \qquad k = \frac{3\,\mu_B\,\mu_0\,N\,I}{2\,R^3}.} \tag{3.9}$$

From equation 3.8 the linear behavior requires the *second term* to be negligible:

$$\frac{5}{2}\left(\frac{\delta z}{R}\right)^2 \ll 1.$$

As in Subsec. 3.2, we activate the force when the bunch center coincides with the coil center, $z_c = z_b$. Over the pulsed region we have $|\delta z| \le \Delta z_{\max} = L/2$, where L is length of the chain. Imposing that the second term $\frac{5}{2}(\delta z/R)^2$ be $\ll 1$ over this interval gives

$$R \gg \sqrt{\frac{5}{2}}\,\Delta z_{\max} = \sqrt{\frac{5}{2}}\,\frac{L}{2} \approx 0.79\,L.$$

Numerical test at $z_b = 10$ cm: We start again with a pointlike bunch (to simplify the problem) and longitudinal velocities $v \in [50, 60]\ \mathrm{m\,s^{-1}}$. The coil is centered at $z_b = 0.10$ m and the detector at 2 m. When the bunch center reaches the coil ($z_c = z_b$, as in Subsec. 3.2), the time is $t_c = z_b/v_c \simeq 0.10/55 \simeq 1.82$ ms. The resulting bunch length at activation is

$$L \approx (v_{\max} - v_{\min})\,t_c = 10 \times \frac{0.10}{55} = \frac{1}{55}\,\mathrm{m} \approx 1.82\ \mathrm{cm}.$$

To enforce near-linearity we chose $R = 3L \simeq 0.0545$ m. With this choice and a pulse when $z_c = z_b$ (activation window 1.818–1.868 ms), the arrival-time spread is reduced from 6.67 ms (no force) to 0.18 ms. However, achieving this temporal focusing with $R \approx 5.45$ cm required $N = 100$ turns and $I \simeq -1900$ A, which is impractical. This is consistent with the scaling from Eq. (3.9), $k = \frac{3\mu_B\mu_0 N I}{2R^3}$: increasing R to improve linearity raises the required NI roughly as R^3, creating a trade-off between linearity and feasibility.

3.3.2 Real coil with realistic current

We now move to the experimental geometry. After the Zeeman–deceleration stage (see Chap. 2), the hydrogen beam forms an initial 3 mm bunch at $z = 0$. We place the pulsed coil at

$$z_b = 0.20\ \mathrm{m},$$

(This choice is explained in the next paragraph) and probe the beam at the detection plane

$$z = 1.00\ \mathrm{m}$$

with a 10 ns laser of 1 mm diameter. In this section we seek coil parameters that are experimentally realistic (current and turns) while still producing temporal focusing at the detector. As before, we trigger the pulse when the bunch center reaches the coil center, $z_c = z_b$, and we model the on-axis field and force with Eqs. (3.4)–(3.6) specialized to the working state $F = 1$, $m_F = 1$.

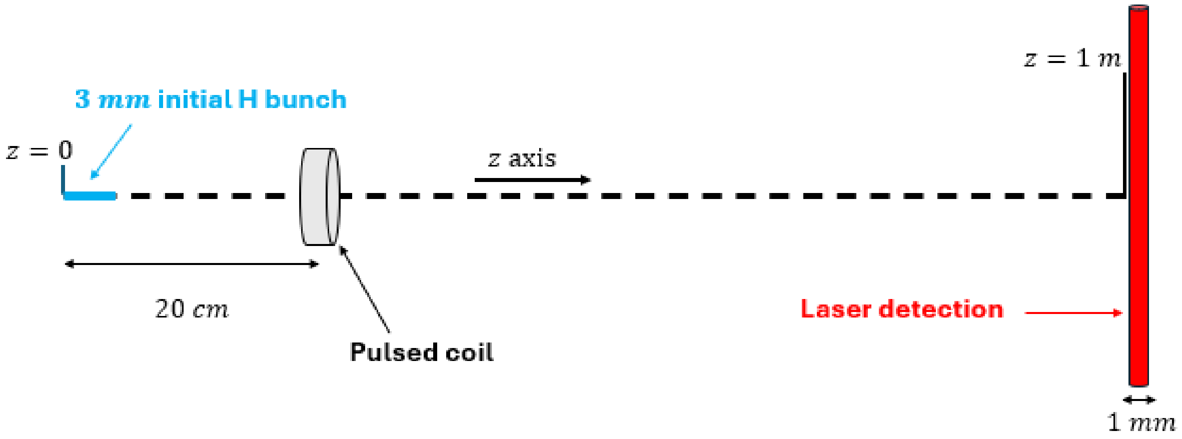

Figure 3.4: Experimental layout: a 3 mm initial H bunch (blue) at $z = 0$, a pulsed coil centered at $z_b = 0.20$ m, and laser detection at $z = 1.00$ m with a 1 mm spot.

Our idea is to choose a coil radius R smaller than the bunch length L at the activation time so that less current is needed, while still focusing a substantial fraction of the beam. Activating earlier is better (shorter L), but we set $z_b = 20$ cm to leave space for the hexapole (see Chap.2). The initial bunch is 3 mm long with random velocities $v \in [50, 60]\ \mathrm{m\,s^{-1}}$. To make temporal focusing possible, we need a position–velocity correlation at activation (atoms ordered by velocity). In the worst case (fastest initially at $z = 0$ and slowest at $z = 3mm$), the ordering time is

$$t_{\mathrm{ord}} = \frac{\Delta z_0}{\Delta v} = \frac{3\ \mathrm{mm}}{10\ \mathrm{m\,s^{-1}}} = 3 \times 10^{-4}\ \mathrm{s} = 0.30\ \mathrm{ms}.$$

During this time the bunch center travels $z \simeq v_c t_{\mathrm{ord}}$ with $v_c \approx 55\ \mathrm{m\,s^{-1}}$, i.e.

$$z \approx 55 \times 0.30\ \mathrm{ms} \approx 1.65\ \mathrm{cm}.$$

Thus activating when the center reaches the coil, $z_c = z_b = 20$ cm, safely meets the ordering requirement.

Instead of fixing the detection, we decided to see where we have z_{peak}: the maximum fraction of atoms (percent) inside a 1 mm window at a given time. For $R = 1$ cm and $\Delta t_{\mathrm{pulse}} = 0.3$ ms,

$$\begin{aligned} NI &= 9.98 \times 10^2\ \mathrm{A\,turns} &\Rightarrow&\quad \text{percent} = 24.7\%, &\quad z_{\mathrm{peak}} &= 0.30\ \mathrm{m}, \\ NI &= 1.41 \times 10^3\ \mathrm{A\,turns} &\Rightarrow&\quad \text{percent} = 30.6\%, &\quad z_{\mathrm{peak}} &= 0.26\ \mathrm{m}. \end{aligned}$$

Increasing NI raises the percentage while shifting the focus upstream (smaller z_{peak}). Given the experimental requirement of at least 50 cm of free space after the coil (because we should leave a space for the $30cm$ length mirror-absorber system), these main peaks are too close; z_{peak} must be pushed downstream (beyond 0.70 m when $z_b = 0.20$ m).

I carried out many simulations by manually exploring parameter sets. As a representative example where the maximum percentage is farther than our first example above, with the coil centered at $z_b = 0.50$ m, choosing $R = 3$ cm, $\Delta t_{\text{pulse}} = 0.3$ ms, and $NI = 2.81 \times 10^3$ A turns, I obtain an optimal peak fraction of 10.2% (within a 1 mm window) at $z_{\text{peak}} = 0.90$ m and $t_{\text{peak}} = 16.6$ ms, i.e. the focus occurs about $z_{\text{peak}} - z_b = 0.40$ m (40 cm) downstream of the coil which is acceptable for instance.

3.3.3 Multiparameter simulation

We now run a multiparameter study. The initial bunch is $L_0 = 3$ mm with velocities $v \in [50, 60]$ $\mathrm{m\,s^{-1}}$. We vary the coil radius over $R \in [3$ mm, 3 cm$]$, the coil position over $z_b \in \{20, 30, 40, 50\}$ cm, and the pulse width over $\Delta t_{\text{pulse}} \in [30, 300]$ μs. Timing follows the rule

$$t_{\text{centrale}} = \frac{z_b - \frac{L_0}{2}}{\bar{v}}, \qquad \bar{v} = \tfrac{1}{2}(v_{\min} + v_{\max}),$$

and we scan $t_{\text{on}} \in [t_{\text{centrale}} - \Delta t_{\text{pulse}},\, t_{\text{centrale}}]$ with $t_{\text{off}} = t_{\text{on}} + \Delta t_{\text{pulse}}$.

For each coil position z_b, we first determine the required “impulsion”

$$\Theta \equiv \frac{NI\,\Delta t_{\text{pulse}}}{R^3},$$

choosing Θ so that the beam focuses at $z = 1$ m. Once $\Theta(z_b)$ is fixed, every simulation point $(R, \Delta t_{\text{pulse}})$ uses

$$NI = \Theta(z_b)\,\frac{R^3}{\Delta t_{\text{pulse}}},$$

and we run all combinations possible for each z_b. We also repeat the full set at each z_b with NI adjusted by ±10%. For each set of parameters, we record the maximum percentage of atoms inside a 1 mm window and the corresponding z_{peak}.

Data analysis. Because the problem is highly multiparameter (z_b, R, Δt_{pulse}, NI, t_{on}), clear trends are not evident. Figure 3.5 reports, for each coil position z_b (noted Z0 on the axis), the *maximum percentage* of atoms found inside the 1 mm window over all tested parameter combinations. The overall maximum percentage is again about 10%. We also observe that the maximum percentage generally decreases as z_b increases, which is natural since the bunch is longer at activation and a smaller portion of the beam lies within the coil's effective region. At $z_b = 50$ cm, we observe an exception: after the first cluster of points—appearing as a continuation of the trend for other z_b—the maximum percentage increases again, reaching about 11%; This behavior is still not understood.

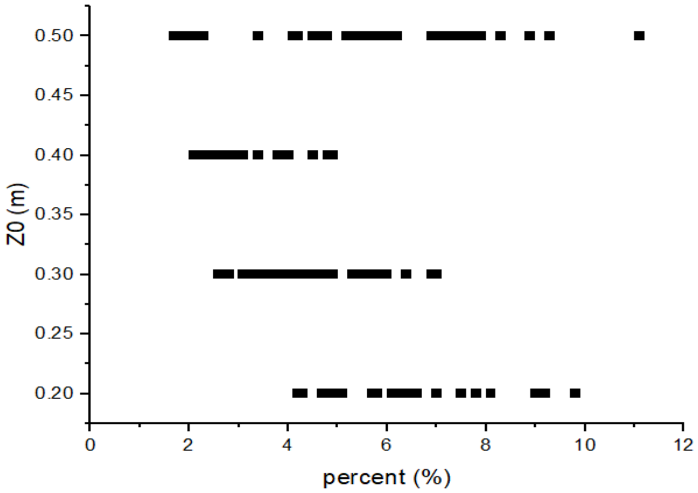

Figure 3.5: Maximum percentage of atoms inside the 1 mm window versus the coil position z_b (labeled Z0). For each z_b, the best value over all tested parameter combinations is shown.

Larger coils clearly perform better: color-coding by R (Fig. 3.6) shows that the highest percentages occur for $R = 0.03$ m (blue), while for $R = 0.003$ m (red) the percentages remain below a few percent. This trend is consistent with the linearization argument—larger R makes the force more nearly linear across the bunch, improving compression for a given impulsion.

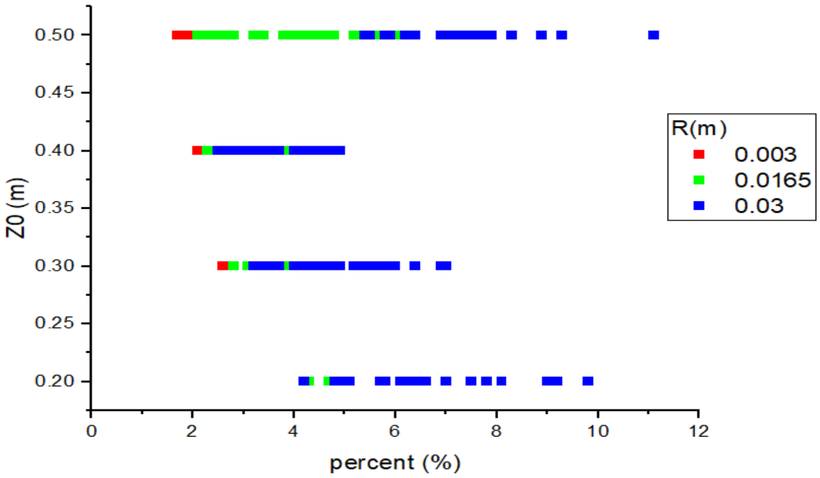

Figure 3.6: Maximum percentage of atoms in the 1 mm window vs. coil position z_b (labeled Z0), color-coded by radius R: $R = 0.003$ m (red), $R = 0.0165$ m (green), $R = 0.03$ m (blue). Larger $R \Rightarrow$ higher percentage, consistent with improved linearity over the bunch.

Figure 3.7 shows that higher percentages coincide with larger NI.

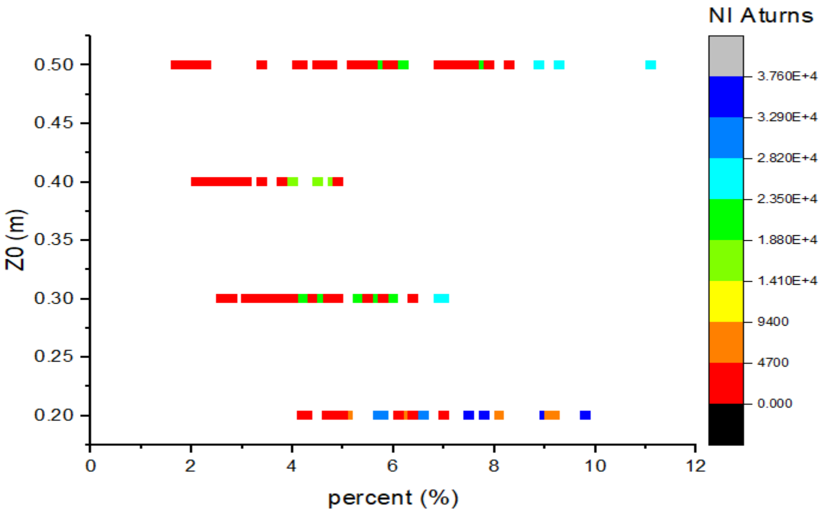

Figure 3.7: Maximum percentage vs. coil position z_b (labeled Z0), color-coded by NI (A·turns).

3.3.4 Phase-space evolution

To better understand the mechanism, we examine the evolution in phase space. For illustration, we randomly select one simulation run from our sweep. That run has

$$z_b = 0.04 \text{ m}, \qquad R = 0.02 \text{ m}, \qquad \Delta t_{\text{pulse}} = 0.3 \text{ ms}, \qquad NI = 1.39 \times 10^3 \text{ A turns},$$

and yields a maximum percentage of 10.2% within the 1 mm window, reached at $t_{\text{peak}} = 12.8$ ms and $z_{\text{peak}} = 0.691$ m.

We now reuse the same coil but compute and use this time the full *3D* magnetic field. The coil we took in simulation is that of a single-turn circular loop carrying a current NI with the same parameters as above; the field formulas are taken from Ref. [9]. The goal is to analyze and see what happens in the transverse directions (x, y) as well. The initial phase-space distribution we took is

$$z \in [0, 3 \text{ mm}], \quad v_z \in [50, 60] \text{ m s}^{-1}, \qquad x, y \in [-0.5, 0.5] \text{ mm}, \quad v_x, v_y \in [-1, 1] \text{ m s}^{-1}.$$

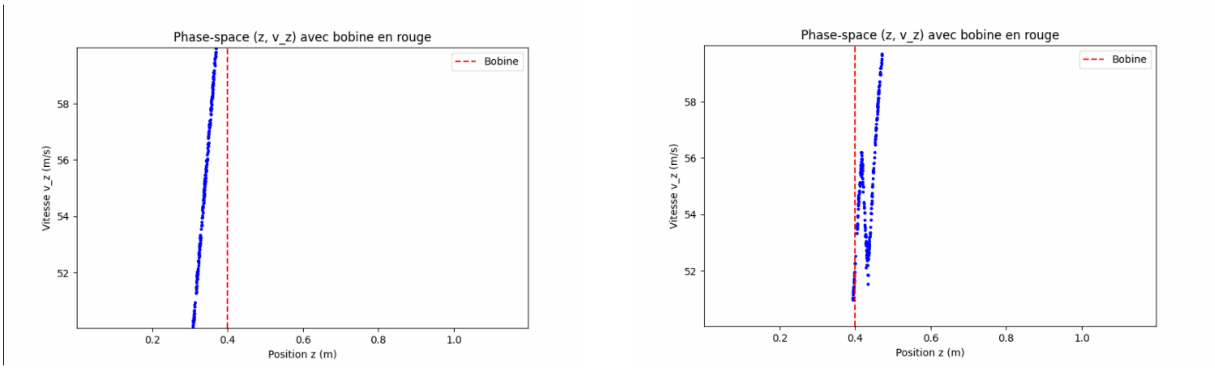

(a) Free flight (before the pulse).

(b) Immediately after the pulse at z_b.

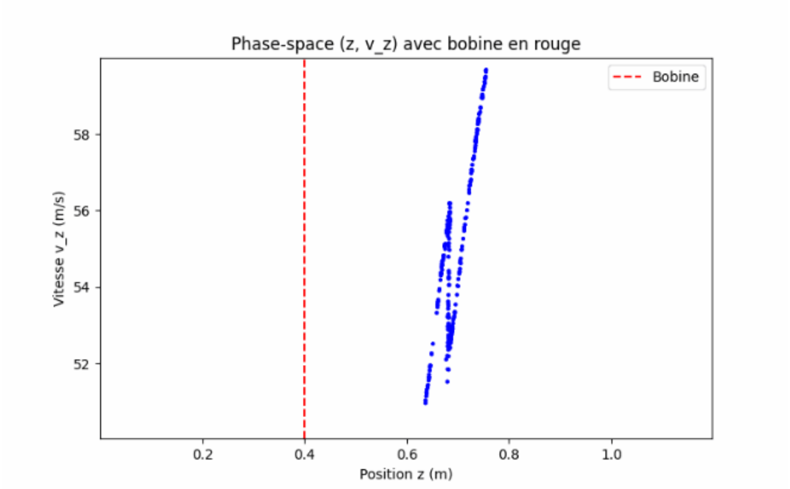

(c) At the focus $z = z_{\text{peak}}$.

Figure 3.8: Evolution in (z, v_z) with the coil position shown by the dashed red line.

We start with an initial bunch of width 3 mm and velocity dispersion between 50 and 60 m/s. After a free flight (Fig. 3.8(a)), atoms with higher velocities move faster along the z-axis, so the initially rectangular distribution in phase space (z, v_z) becomes tilted. This produces a clear correlation between position and velocity, as expected.

When a localized pulse is applied(Fig. 3.8(b)), it acts only on a part of the atomic beam. In phase space, this corresponds to an inversion of the slope of a part of the distribution.

After another free flight, the ensemble evolves such that the distribution refocuses: the atoms converge again in space, despite their initial velocity spread. The focalization is maximal when the distribution in (z, v_z) becomes vertical, meaning that atoms with different initial velocities arrive at the same spatial position simultaneously (Fig. 3.8(c)).

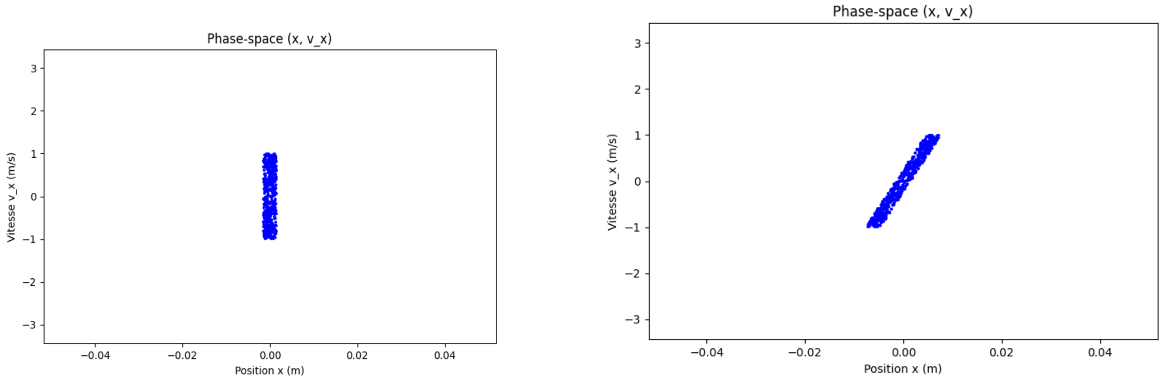

(a) Initial distribution (x, v_x).

(b) After free flight (before the pulse).

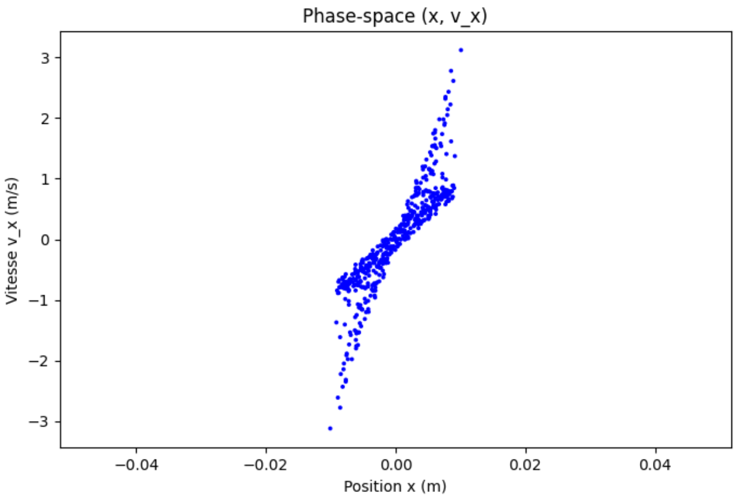

(c) Just after the pulse.

Figure 3.9: Evolution in the transverse phase space (x, v_x).

[1]

By cylindrical symmetry the same behavior holds in (y, v_y): the core of the cloud stays within $|v_{x,y}| \lesssim 1\ \mathrm{m\,s^{-1}}$, while a small fraction is driven transversely to $|v_{x,y}| \sim 3\ \mathrm{m\,s^{-1}}$.

3.4 Conclusion and outlook

Our target was a detection fraction of $\sim 33\%$, since the laser spot is 1 mm while the initial bunch length is 3 mm. The study is well advanced but still requires optimization. At present we reach $\sim 10\%$. The main reason is geometric: at the activation time we chose coil radius R smaller than the bunch length L (because we don't want high NI unfeasible as explained before), so the pulse acts only on a portion of the bunch rather than on all atoms.

An interesting idea is to insert a second hexapole stage after the first one in Fig. 2.1, acting as a phase–space rotator shortly after $t = 0$, so that the longitudinal distribution does not expand before the pulsed coil is triggered. This option remains to be studied in detail and was not pursued further here due to time constraints.

---

[1] The symmetry of the distribution is conserved; see App. E.

Chapter 4

My experimental work

4.1 Initial orientation and objectives

At the beginning of my internship, Dr. Martin Simon (University of Vienna) visited our lab and walked me through each part of the experimental setup. My assignment was to design, model, and integrate a radiative heat shield. At that time, the system operated around 14 K, whereas in Chapter 2 we established a target temperature of 6 K for the stage hosting the hydrogen beam. The heat shield was therefore designed to suppress incoming blackbody radiation onto the beam stage and thus to be cooled to approximately 6 K.

Along the way, I gained practical experience with vacuum hardware and cryogenic practices, as well as hands-on skills such as soldering. For example, we cut and re-terminated the leads of a temperature sensor and then re-soldered them during the rerouting of the wiring.

4.1.1 Two-stage cryocooler

Figure 4.1: Two-stage cryocooler used to cool the experimental beam stage.

This two-stage regenerative cryocooler uses a Stirling-type refrigeration cycle with helium gas. A room-temperature compressor produces alternating high/low pressure, while valves (or a phase shifter) set the right timing. Each stage contains a regenerator—a porous matrix with high heat capacity—that stores heat on the way down and returns it on the way back. During the high-pressure stroke the gas flows through the regenerator, is precooled to the local cold-end temperature, and reaches the cold heat exchanger. There it undergoes an effectively isothermal expansion and absorbs the thermal load $\dot{Q}_c$ from the attached sample. During the low-pressure stroke the gas returns through the regenerator, picks up the stored heat, and rejects it at the warm end. Stage 1 (60–80 K) intercepts radiation/conduction from 300 K and precools the stream feeding Stage 2. Stage 2 (4–10 K) provides the ultracold tip; its rejected heat is dumped into Stage 1, which then rejects to ambient. Repeating cycles pump small packets of enthalpy each time, so the cold masses cool down gradually until the cooling power balances the load. Real machines achieve a fraction of Carnot efficiency due to finite effectiveness of the regenerator, pressure drops, phasing losses, and parasitic heat leaks.

4.1.2 First heat shield

To suppress black–body radiation onto the second stage, we installed a copper heat shield thermally anchored to the first stage ($\sim$60–80 K). The radiative heat leak to a surface at temperature T_c is

$$\dot{Q}_{\text{rad}} = \varepsilon\,\sigma A\big(T_{\text{view}}^4 - T_c^4\big)\,, \tag{4.1}$$

with emissivity ε, area A, and the Stefan–Boltzmann constant σ. Without a shield the cold tip "sees" $T_{\text{view}} \approx 300\,\text{K}$; after installing the shield the view temperature drops to $T_{\text{view}} \approx 60\,\text{K}$, giving

$$\frac{\dot{Q}_{\text{rad}}^{(60\,\text{K})}}{\dot{Q}_{\text{rad}}^{(300\,\text{K})}} \simeq \frac{60^4 - T_c^4}{300^4 - T_c^4} \approx 1.6 \times 10^{-3} \quad (T_c \approx 12\,\text{K}). \tag{4.2}$$

Consistently, the base temperature improved from $\sim$14 K (no shield) to the value shown in Fig. 4.3, $T_c = 11.861\,\text{K}$ (Channel A). In practice, polished or gold-plated shields further reduce ε, lowering the radiative load. Figure 4.2 shows the mechanical design with SolidWorks + the shield installed; the improved base temperature is confirmed in Fig. 4.3.

(a) HBEAM first heat shield: mechanical design (SolidWorks).

(b) The heat shield installed.

Figure 4.2: First heat shield.

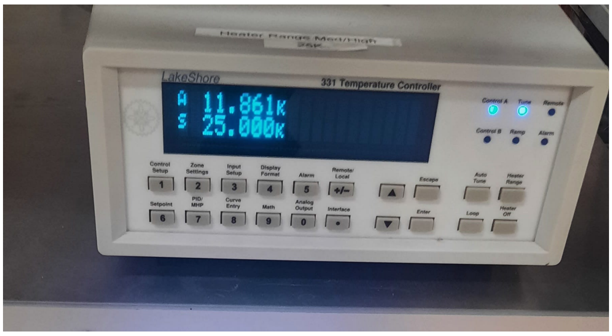

Figure 4.3: Lakeshore controller readout after installing the shield: $T_c = 11.861\,\mathrm{K}$.

4.1.3 Double heat shield

Because we did not reach 6 K with the single shield, we redesigned a *double* heat shield with an inner and an outer enclosure, and added more screws to improve thermal contact. After installation and cooldown, the base temperature remained essentially unchanged at $T_c \simeq 11.9\,\mathrm{K}$. From the outset, I questioned the cryocooler's capacity and overall performance. We measured the helium line pressure at $\sim$ 14 bar, below the nominal 15.7 bar, and initially considered a refill. However, checking the manufacturer's information for the Sumitomo CH-210 showed that the minimum second-stage temperature is about 10 K (see Fig 4.5). Dr. Martin, who had worked with the setup for spectroscopic measurements before, told us that our cryostat is supposed to reach 4 K. We trusted his word and used heat shields, but yes, we should have checked from the beginning. Therefore, a 6 K target is not achievable with this unit; the observed $\sim$11.9 K is consistent with the model's specification and remaining conductive/radiative loads.

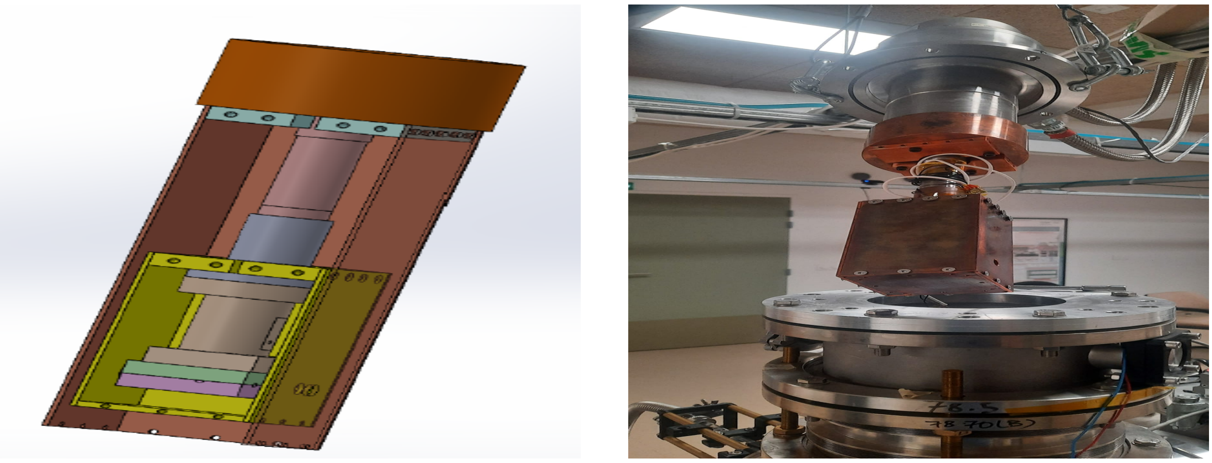

(a) CAD of the double (inner+outer) heat shield.

(b) Inner heat shield installed.

Figure 4.4: Double heat-shield concept and mechanical design and inner shield installed shown.

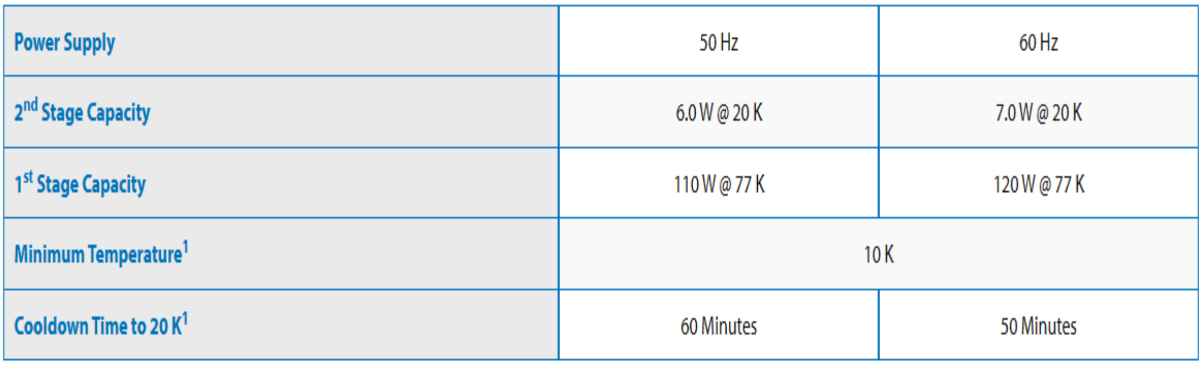

Power Supply	50 Hz	60 Hz
2nd Stage Capacity	6.0 W @ 20 K	7.0 W @ 20 K
1st Stage Capacity	110 W @ 77 K	120 W @ 77 K
Minimum Temperature[1]	10 K	
Cooldown Time to 20 K[1]	60 Minutes	50 Minutes

Figure 4.5: CH-210 10K Cryocooler .

Appendix A

Definition of a Linear Magnetic Field

We seek to define a static magnetic field $\vec{B}$ in the following general linear form:

$$\vec{B} = B_x(x,y,z)\,\vec{e}_x + B_y(x,y,z)\,\vec{e}_y + B_z(x,y,z)\,\vec{e}_z \tag{A.1}$$

with:

$$B_x(x,y,z) = B_0^x + \alpha x + \beta y + \gamma z \tag{A.2}$$
$$B_y(x,y,z) = B_0^y + \delta x + \epsilon y + \zeta z \tag{A.3}$$
$$B_z(x,y,z) = B_0^z + \eta x + \theta y + \kappa z \tag{A.4}$$

where $B_0^x, B_0^y, B_0^z, \alpha, \beta, \gamma, \delta, \epsilon, \zeta, \eta, \theta, \kappa$ are constants.

Condition 1: Zero divergence
The magnetic field must satisfy:

$$\nabla \cdot \vec{B} = \frac{\partial B_x}{\partial x} + \frac{\partial B_y}{\partial y} + \frac{\partial B_z}{\partial z} = 0 \tag{A.5}$$

which imposes the constraint:

$$\alpha + \epsilon + \kappa = 0 \tag{A.6}$$

Condition 2: Zero curl
The magnetic field must also satisfy:

$$\nabla \times \vec{B} = \vec{0} \tag{A.7}$$

This leads to the following component-wise constraints:

$$\frac{\partial B_z}{\partial y} - \frac{\partial B_y}{\partial z} = 0 \quad \Rightarrow \quad \theta = \zeta \tag{A.8}$$
$$\frac{\partial B_x}{\partial z} - \frac{\partial B_z}{\partial x} = 0 \quad \Rightarrow \quad \gamma = \eta \tag{A.9}$$
$$\frac{\partial B_y}{\partial x} - \frac{\partial B_x}{\partial y} = 0 \quad \Rightarrow \quad \delta = \beta \tag{A.10}$$

Final Form of the Field

Thus, the magnetic field becomes:

$$\boxed{\vec{B} = (B_0^x + \alpha x + \beta y + \gamma z)\,\vec{e}_x + (B_0^y + \beta x + \epsilon y + \theta z)\,\vec{e}_y + (B_0^z + \gamma x + \theta y + \kappa z)\,\vec{e}_z} \tag{A.11}$$

with the constraints:

$$\alpha + \epsilon + \kappa = 0, \quad \delta = \beta, \quad \zeta = \theta, \quad \eta = \gamma \tag{A.12}$$

Full Expression of the Magnetic Field Norm and Associated Force

The norm of the magnetic field is:

$$\|\vec{B}\| = \sqrt{B_x^2 + B_y^2 + B_z^2} \tag{A.13}$$

We denote:

$$B_x = B_0^x + \alpha x + \beta y + \gamma z \tag{A.14}$$

$$B_y = B_0^y + \beta x + \epsilon y + \theta z \tag{A.15}$$

$$B_z = B_0^z + \gamma x + \theta y + \kappa z \tag{A.16}$$

Each squared component expands as follows:
1. B_x^2:

$$\begin{aligned} B_x^2 &= (B_0^x + \alpha x + \beta y + \gamma z)^2 \\ &= (B_0^x)^2 + 2B_0^x(\alpha x + \beta y + \gamma z) \\ &\quad + \alpha^2 x^2 + \beta^2 y^2 + \gamma^2 z^2 + 2\alpha\beta xy + 2\alpha\gamma xz + 2\beta\gamma yz \end{aligned} \tag{A.17}$$

2. B_y^2:

$$\begin{aligned} B_y^2 &= (B_0^y + \beta x + \epsilon y + \theta z)^2 \\ &= (B_0^y)^2 + 2B_0^y(\beta x + \epsilon y + \theta z) \\ &\quad + \beta^2 x^2 + \epsilon^2 y^2 + \theta^2 z^2 + 2\beta\epsilon xy + 2\beta\theta xz + 2\epsilon\theta yz \end{aligned} \tag{A.18}$$

3. B_z^2:

$$\begin{aligned} B_z^2 &= (B_0^z + \gamma x + \theta y + \kappa z)^2 \\ &= (B_0^z)^2 + 2B_0^z(\gamma x + \theta y + \kappa z) \\ &\quad + \gamma^2 x^2 + \theta^2 y^2 + \kappa^2 z^2 + 2\gamma\theta xy + 2\gamma\kappa xz + 2\theta\kappa yz \end{aligned} \tag{A.19}$$

Total Norm Expression:
Let us denote $\|\vec{B}\| = \sqrt{S(x,y,z)}$, where:

$$S(x,y,z) = A_x x^2 + A_y y^2 + A_z z^2 + A_{xy} xy + A_{xz} xz + A_{yz} yz + B_x x + B_y y + B_z z + C \tag{A.20}$$

with the coefficients:

Constant term:

$$C = (B_0^x)^2 + (B_0^y)^2 + (B_0^z)^2 \tag{A.21}$$

Linear coefficients:

$$B_x = 2(\alpha B_0^x + \beta B_0^y + \gamma B_0^z) \tag{A.22}$$
$$B_y = 2(\beta B_0^x + \epsilon B_0^y + \theta B_0^z) \tag{A.23}$$
$$B_z = 2(\gamma B_0^x + \theta B_0^y + \kappa B_0^z) \tag{A.24}$$

Quadratic coefficients:

$$A_x = \alpha^2 + \beta^2 + \gamma^2 \tag{A.25}$$
$$A_y = \beta^2 + \epsilon^2 + \theta^2 \tag{A.26}$$
$$A_z = \gamma^2 + \theta^2 + \kappa^2 \tag{A.27}$$
$$A_{xy} = 2(\alpha\beta + \beta\epsilon + \gamma\theta) \tag{A.28}$$
$$A_{xz} = 2(\alpha\gamma + \beta\theta + \gamma\kappa) \tag{A.29}$$
$$A_{yz} = 2(\beta\gamma + \epsilon\theta + \theta\kappa) \tag{A.30}$$

Associated Force:
The associated force is defined as:

$$\vec{F} = -\nabla\|\vec{B}\| = -\frac{1}{2\sqrt{S(x,y,z)}}\nabla S(x,y,z) \tag{A.31}$$

Explicitly:

$$\boxed{\vec{F}(x,y,z) = -\frac{1}{2\sqrt{S(x,y,z)}}\begin{pmatrix}2A_x x + A_{xy}y + A_{xz}z + B_x\\ 2A_y y + A_{xy}x + A_{yz}z + B_y\\ 2A_z z + A_{xz}x + A_{yz}y + B_z\end{pmatrix}} \tag{A.32}$$

Simulation Parameters and Observations

In the simulations, the magnetic field is implemented using this full analytical expression. Using *Mathematica*, we solved the equations of motion for atoms subjected to such a force, using various values of the coefficients above. Below is a representation of the interactive slider interface used to explore these parameters:

Despite extensive parameter sweeps, both manually and automatically, no decrease in the area of the convex hull was ever observed in either the (x, v_x) or (y, v_y) subspaces.

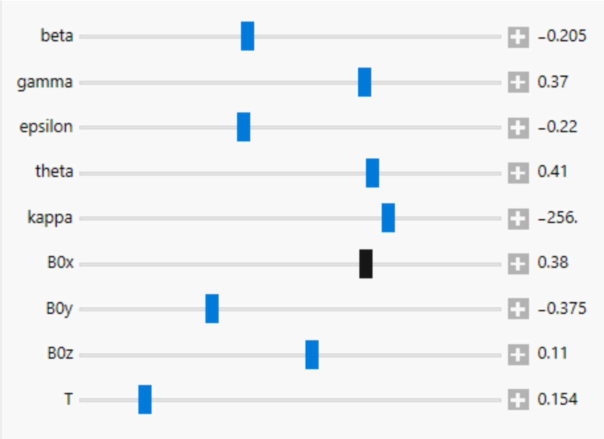

beta −0.205
gamma 0.37
epsilon −0.22
theta 0.41
kappa −256.
B0x 0.38
B0y −0.375
B0z 0.11
T 0.154

Figure A.1: Sliders used to manually adjust magnetic field parameters and duration T of the simulation.

Appendix B

Theoretical part of Chapter 2

B.1 Conservation of the global inversion symmetry in linear case

We aim to prove that if a particle density $\rho(x, v_x, y, v_y, t)$ is initially symmetric under simultaneous inversion of all variables, i.e.:

$$\rho_0(-x, -v_x, -y, -v_y) = \rho_0(x, v_x, y, v_y), \tag{B.1}$$

then this symmetry is preserved at all times t under the action of a linear force of the form:

$$F_x = cx + ay, \qquad F_y = ax + by. \tag{B.2}$$

We work in the phase space $\mathbb{R}^4$ with the state vector:

$$Z = \begin{pmatrix} x \\ v_x \\ y \\ v_y \end{pmatrix}, \tag{B.3}$$

and a linear dynamics given by:

$$\frac{dZ}{dt} = MZ, \quad \text{where } M = \begin{pmatrix} 0 & 1 & 0 & 0 \\ c & 0 & a & 0 \\ 0 & 0 & 0 & 1 \\ a & 0 & b & 0 \end{pmatrix}. \tag{B.4}$$

The solution to this system is:

$$Z(t) = e^{tM} Z(0). \tag{B.5}$$

The phase-space density at time t is given by:

$$\rho(Z, t) = \rho_0(e^{-tM} Z), \tag{B.6}$$

since the flow is deterministic, linear, and volume-preserving (Liouville's theorem).

We assume that:

$$\rho_0(QZ) = \rho_0(Z) \quad \text{with } Q = \mathrm{diag}(-1, -1, -1, -1). \tag{B.7}$$

This corresponds to a global inversion:

$$QZ = (-x, -v_x, -y, -v_y). \tag{B.8}$$

We want to prove that this symmetry is preserved over time, i.e.:

$$\rho(QZ, t) = \rho(Z, t) \quad \text{for all } t \in \mathbb{R}. \tag{B.9}$$

We begin by writing:

$$\rho(QZ, t) = \rho_0(e^{-tM} QZ). \tag{B.10}$$

If we can show that:

$$e^{-tM} QZ = Qe^{-tM} Z, \tag{B.11}$$

then it follows that:

$$\rho(QZ, t) = \rho_0(Qe^{-tM} Z). \tag{B.12}$$

And using the initial symmetry hypothesis:

$$\rho_0(Qe^{-tM} Z) = \rho_0(e^{-tM} Z) = \rho(Z, t). \tag{B.13}$$

Let:

$$Q = \operatorname{diag}(-1, -1, -1, -1), \quad \text{so } Q = -I. \tag{B.14}$$

We compute:

$$QM = (-I)M = -M, \quad MQ = M(-I) = -M \Rightarrow QM = MQ. \tag{B.15}$$

Thus:

$$[Q, M] = QM - MQ = 0 \quad \Rightarrow \quad Qe^{-tM} = e^{-tM} Q. \tag{B.16}$$

Hence:

$$e^{-tM} QZ = Qe^{-tM} Z. \tag{B.17}$$

We conclude that:

$$\rho(QZ, t) = \rho_0(e^{-tM} QZ) = \rho_0(Qe^{-tM} Z) = \rho_0(e^{-tM} Z) = \rho(Z, t). \tag{B.18}$$

The global symmetry of the initial density is therefore rigorously preserved at all times t.

This result relies on two fundamental facts:

- The evolution of $Z(t)$ is linear, given by e^{tM}.
- The symmetry matrix Q commutes with M: $[Q, M] = 0$.

B.2 An equation for the marginal density $\rho_y(y, v_y, t)$

The marginal density $\rho_y(y, v_y, t)$ is defined by:

$$\rho_y(y, v_y, t) = \int dx\, dv_x\, \rho(x, y, v_x, v_y, t) \tag{B.19}$$

Liouville equation

$$\frac{\partial \rho}{\partial t} + \vec{v} \cdot \nabla_{\vec{r}} \rho + \frac{\vec{F}}{m} \cdot \nabla_{\vec{v}} \rho = 0 \tag{B.20}$$

where $\rho = \rho(x, y, v_x, v_y, t)$, $\vec{r} = (x, y)$, $\vec{v} = (v_x, v_y)$, and $\vec{F} = -\nabla_{\vec{r}} V(x, y)$.

Integration of the Liouville equation over x and v_x

We integrate:

$$\int dx\, dv_x \left(\frac{\partial \rho}{\partial t} + v_x \frac{\partial \rho}{\partial x} + v_y \frac{\partial \rho}{\partial y} + \frac{F_x}{m} \frac{\partial \rho}{\partial v_x} + \frac{F_y}{m} \frac{\partial \rho}{\partial v_y} \right) = 0 \tag{B.21}$$

Term-by-term, we get:

$$\int dx\, dv_x \frac{\partial \rho}{\partial t} = \frac{\partial \rho_y}{\partial t} \tag{B.22}$$

$$\int dx\, dv_x\, v_y \frac{\partial \rho}{\partial y} = v_y \frac{\partial \rho_y}{\partial y} \tag{B.23}$$

$$\int dx\, dv_x \frac{F_y}{m} \frac{\partial \rho}{\partial v_y} = \frac{1}{m} \int dx\, dv_x\, F_y \frac{\partial \rho}{\partial v_y} \tag{B.24}$$

And assuming fast decay at infinity:

$$\int dx\, dv_x\, v_x \frac{\partial \rho}{\partial x} = 0 \tag{B.25}$$

$$\int dx\, dv_x \frac{F_x}{m} \frac{\partial \rho}{\partial v_x} = 0 \tag{B.26}$$

(see Appendix C for justification of the last two integrals). Therefore, we obtain:

$$\frac{\partial \rho_y}{\partial t} + v_y \frac{\partial \rho_y}{\partial y} + \frac{1}{m} \int dx\, dv_x\, F_y(x, y) \frac{\partial \rho}{\partial v_y} = 0 \tag{B.27}$$

Special case: force independent of x

If the force is of the form $\vec{F}(y) = -\partial_y V(y)$, i.e., depends only on y, then:

$$\frac{\partial \rho_y}{\partial t} + v_y \frac{\partial \rho_y}{\partial y} + \frac{F_y(y)}{m} \frac{\partial \rho_y}{\partial v_y} = 0 \tag{B.28}$$

This is a Liouville equation *in the subspace* (y, v_y), provided the force depends only on y. This corresponds to a decoupling of the longitudinal and transverse dynamics. This explains why the area is conserved in two subspaces separately in Figures 2.9 and 2.10.

Appendix C

Justification of the cancellation of two integrals

We want to show that, under the assumption that the probability density $\rho(x, y, v_x, v_y, t)$ decays sufficiently fast at infinity, the following two integrals vanish.

1. Term $\int dx\, dv_x\, v_x \frac{\partial \rho}{\partial x}$

We perform integration by parts with respect to x, treating v_x as constant in the inner integral:

$$\begin{aligned} \int dx\, dv_x\, v_x \frac{\partial \rho}{\partial x} &= \int dv_x \left(\int dx\, v_x \frac{\partial \rho}{\partial x} \right) \\ &= \int dv_x \, \left[v_x \rho \right]_{x=-\infty}^{x=+\infty} - \int dv_x \left(\int dx\, \frac{\partial v_x}{\partial x} \rho \right) \end{aligned} \tag{C.1}$$

Since $\partial v_x / \partial x = 0$, this simplifies to:

$$\int dx\, dv_x\, v_x \frac{\partial \rho}{\partial x} = \int dv_x \, \left[v_x \rho(x, y, v_x, v_y) \right]_{x=-\infty}^{x=+\infty} \tag{C.2}$$

Assuming that $\rho \to 0$ as $x \to \pm\infty$, the boundary term vanishes, and thus:

$$\boxed{\int dx\, dv_x\, v_x \frac{\partial \rho}{\partial x} = 0} \tag{C.3}$$

2. Term $\int dx\, dv_x\, \frac{F_x(x, y)}{m} \frac{\partial \rho}{\partial v_x}$

Here, $F_x(x, y)/m$ is independent of v_x, so we factor it out and integrate by parts in v_x:

$$\begin{aligned} \int dx\, dv_x\, \frac{F_x(x, y)}{m} \frac{\partial \rho}{\partial v_x} &= \int dx\, \frac{F_x(x, y)}{m} \left[\int dv_x\, \frac{\partial \rho}{\partial v_x} \right] \\ &= \int dx\, \frac{F_x(x, y)}{m} \, \left[\rho \right]_{v_x=-\infty}^{v_x=+\infty} \end{aligned} \tag{C.4}$$

Under the assumption that $\rho \to 0$ when $v_x \to \pm\infty$, we find:

$$\boxed{\int dx\, dv_x\, \frac{F_x(x,y)}{m} \frac{\partial \rho}{\partial v_x} = 0} \tag{C.5}$$

Appendix D

Symplectic Geometry and Gromov's Non-Squeezing Theorem

> *"Symplectic geometry is the language of Classical Mechanics in its Hamiltonian formulation,*
> *and it also plays a crucial role in Quantum Mechanics."*

After discovering the constraints imposed by Gromov's theorem on distributions in phase space—and because it is less well known than Liouville's theorem yet more powerful—I devoted one month of my internship to understanding symplectic geometry. I then gave a group seminar entitled "Symplectic Geometry Demystified," and this chapter is essentially a concise version of that presentation.

D.1 The Mystery of the Symplectic Egg

Take a hard-boiled egg and slice it across its widest part: the resulting cross-section is a circle of area

$$A = \pi r^2. \tag{D.1}$$

If, instead, you cut the egg along a longitudinal plane, the section is an ellipse whose area is

$$A = \pi R^2, \tag{D.2}$$

which is strictly larger.

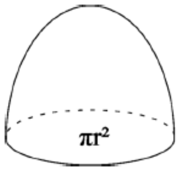

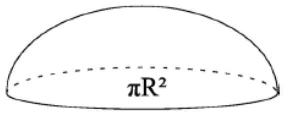

By contrast, for a *symplectic egg*—an ellipsoid obtained from a ball via a linear symplectic transformation—*every* slice that passes through the centre, provided the cutting plane is a plane of conjugate coordinates, has the *same* area.

A symplectic egg is simply the image of a ball under a linear symplectic transformation. Remarkably, if the radius of a symplectic egg is chosen as $\sqrt{\hbar}$, every central cross-section has area

$$\pi\hbar \;=\; \frac{h}{2}. \tag{D.3}$$

This value coincides with the minimal action cell dictated by the quantum-mechanical uncertainty principle.

D.2 Symplectic Geometry

D.2.1 The Standard Symplectic Matrix

The symplectic structure on $\mathbb{R}^{2n}$ is encoded in the matrix

$$J \;=\; \begin{pmatrix} 0 & I_n \\ -I_n & 0 \end{pmatrix}, \tag{D.4}$$

where I_n is the $n \times n$ identity matrix. It satisfies

$$J^2 = -I_{2n}, \qquad J^T = J^{-1} = -J. \tag{D.5}$$

Together, (D.4)–(D.5) define the geometry of phase space.

D.2.2 Analogy Between Euclidean and Symplectic Geometry

Euclidean Geometry and Orthogonal Matrices

Euclidean geometry studies linear maps that preserve the inner product

$$\langle u, v\rangle = u^T v. \tag{D.6}$$

A matrix M preserves lengths precisely when

$$\langle Mu, Mv\rangle = \langle u, v\rangle \iff M^T I M = I, \tag{D.7}$$

and such matrices are called *orthogonal*.

Symplectic Geometry and Symplectic Matrices

Symplectic geometry replaces the inner product by the *symplectic product*

$$z \wedge z' \;=\; (z')^T J z. \tag{D.8}$$

A matrix S preserves this form iff

$$(Sz) \wedge (Sz') = z \wedge z' \iff S^T J S = J, \tag{D.9}$$

and such matrices are called *symplectic*.

D.2.3 Symplectic Matrices

Definition: A real $2n \times 2n$ matrix S is symplectic if

$$S^T J S = J. \tag{D.10}$$

One degree of freedom ($n = 1$): For $n = 1$, (D.10) reduces to

$$\det S = 1. \tag{D.11}$$

Block form: Writing

$$S = \begin{pmatrix} A & B \\ C & D \end{pmatrix}, \qquad A, B, C, D \in \mathbb{R}^{n\times n}, \tag{D.12}$$

the condition (D.10) is equivalent to

$$A^T C = C^T A, \qquad B^T D = D^T B, \qquad A^T D - C^T B = I_n. \tag{D.13}$$

These identities generalise (D.11) to higher dimensions.

Properties of Symplectic Matrices

1. **Closure under multiplication.** If $S, S' \in \mathrm{Sp}(2n, \mathbb{R})$ satisfy (D.10), then

   $$(SS')^T J(SS') = S'^T (S^T JS)S' = S'^T JS' = J, \tag{D.14}$$

   hence the product SS' is symplectic.

2. **Determinant and invertibility.** Taking determinants of (D.10) gives

   $$(\det S)^2 \det J = \det J \implies (\det S)^2 = 1. \tag{D.15}$$

   Thus $\det S = \pm 1$ and every symplectic matrix is invertible. It turns out that in fact $\det S = 1$. This can be proved by more advanced methods.

3. **Inverse is symplectic.** Equation (D.10) implies $JS = (S^{-1})^T J$, so

   $$(S^{-1})^T J\, S^{-1} = J, \tag{D.16}$$

   i.e. $S^{-1} \in \mathrm{Sp}(2n, \mathbb{R})$.

4. **Transposition property.** The symplectic group is closed under transposition—if S is symplectic, so is S^{T}. Taking the inverse of eq. D.16 gives

   $$SJ\big[(S^{-1})^{\mathsf{T}}\big]^{-1} = J,$$

   since $J^{-1} = -J$. And since $\big[(S^{-1})^{\mathsf{T}}\big]^{-1} = S^{\mathsf{T}}$,

   $$SJS^{\mathsf{T}} = J. \tag{D.17}$$

   Thus S^{T} itself satisfies the symplectic condition.

5. **Equivalent block conditions.** Inserting the block form (D.12) into (D.17) gives

   $$AB^{\mathsf{T}} = BA^{\mathsf{T}}, \quad CD^{\mathsf{T}} = DC^{\mathsf{T}}, \quad AD^{\mathsf{T}} - BC^{\mathsf{T}} = I_n. \tag{D.18}$$

   These relations are fully equivalent to the set in (D.13).

Inverse in block form. Because both S^{-1} and $\left(S^{-1}\right)^{\mathsf{T}}$ are symplectic, the inverse of S in the block notation (D.12) is

$$S^{-1} = \begin{pmatrix} D^{\mathsf{T}} & -B^{\mathsf{T}} \\ -C^{\mathsf{T}} & A^{\mathsf{T}} \end{pmatrix}. \tag{D.19}$$

Relation to the 2×2 case. For $n = 1$, (D.19) reduces to the familiar inverse of a 2×2 matrix with unit determinant,

$$\begin{pmatrix} a & b \\ c & d \end{pmatrix}^{-1} = \begin{pmatrix} d & -b \\ -c & a \end{pmatrix},$$

highlighting that symplectic matrices mimic the area-preserving behaviour of 2×2 matrices. Symplectic geometry is, at its core, a geometry of *areas*—a fact that will reappear in Gromov's non-squeezing theorem and the symplectic-egg property.

A remark on determinants and counterexamples. Not every $2n \times 2n$ matrix with determinant one is symplectic when $n > 1$. For instance, consider

$$M = \begin{pmatrix} \lambda & 0 & 0 & 0 \\ 0 & 1/\lambda & 0 & 0 \\ 0 & 0 & \lambda & 0 \\ 0 & 0 & 0 & 1/\lambda \end{pmatrix}, \qquad \lambda \neq 0. \tag{D.20}$$

This matrix has $\det(M) = 1$, but violates the condition

$$AD^{\mathsf{T}} - BC^{\mathsf{T}} = I_d \tag{D.21}$$

unless $\lambda = \pm 1$.

D.2.4 The First Poincaré Invariant

Loop in phase space. Let $\gamma : [0, 2\pi] \to \mathbb{R}^2$ be the closed curve

$$\gamma(t) = \begin{pmatrix} x(t) \\ p(t) \end{pmatrix}, \qquad 0 \leq t \leq 2\pi, \tag{D.22}$$

with $x(0) = x(2\pi)$ and $p(0) = p(2\pi)$; the functions $x(t)$ and $p(t)$ are assumed C^1.

Definition. The *first Poincaré invariant* of γ is the line integral

$$I(\gamma) = \oint_{\gamma} p\,dx = \int_0^{2\pi} p(t)^{\mathrm{T}}\,\dot{x}(t)\,dt, \tag{D.23}$$

which equals the signed area enclosed by the loop in the (x, p)-plane.

Symplectic invariance. If S is any symplectic matrix and we replace the loop by $S\gamma(t)$, $I(\gamma)$ is unchanged:

$$I(\gamma) = \oint_{\gamma} p\,dx = I(S\gamma) = \oint_{S\gamma} p\,dx. \tag{D.24}$$

Thus $I(\gamma)$ is preserved under all linear symplectic transformations.

D.3 Proof of the Symplectic–Egg Property

1. Ball and symplectic egg. Let

$$B_R = \{z = (x,p) \in \mathbb{R}^{2n} \mid |z|^2 = |x|^2 + |p|^2 \le R^2\}. \tag{D.25}$$

For any symplectic matrix S, its image

$$S(B_R) = \{z' \mid |S^{-1}z'| \le R\} \tag{D.26}$$

is an ellipsoid called a *symplectic egg.*

2. Section by a conjugate plane. Intersect $S(B_R)$ with the conjugate plane $\Pi_j \equiv \{x_k = p_k = 0\ (k \ne j)\}$; the intersection is an ellipse Γ_j with boundary loop γ_j. Relabeling coordinates, take $j = 1$ and parameterise

$$\gamma_1(t) = \big(x_1(t), 0, \dots, 0, p_1(t), 0, \dots, 0\big)^{\mathsf{T}}, \qquad 0 \le t \le 2\pi, \tag{D.27}$$

with $x_1(0) = x_1(2\pi)$, $p_1(0) = p_1(2\pi)$.

3. Elliptic-section area. Because $x_k(t) = p_k(t) = 0$ for $k > 1$,

$$\text{Area}(\Gamma_1) = \int_0^{2\pi} p_1(t)\,\dot{x}_1(t)\,dt = \sum_{k=1}^{n} \int_0^{2\pi} p_k(t)\,\dot{x}_k(t)\,dt = \oint_{\gamma_1} p\,dx = I(\gamma_1), \tag{D.28}$$

i.e. the area equals the first Poincaré invariant of the loop.

4. Symplectic invariance and conclusion. The matrix S^{-1} is symplectic, so $I(\gamma_1) = I(S^{-1}\gamma_1)$. The loop $S^{-1}\gamma_1$ lies in the plane $S^{-1}\Pi_1$ and bounds a section of the ball B_R; it is a great circle, whose enclosed area is exactly πR^2. Hence $\text{Area}(\Gamma_1) = \pi R^2$, showing that *every central conjugate slice of a symplectic egg has area* πR^2, which proves the symplectic-egg property.

Illustrative counterexample (why "conjugate & symplectic" matter). Take the symplectic matrix

$$S = \begin{pmatrix} \lambda_1 & 0 & 0 & 0 \\ 0 & \lambda_2 & 0 & 0 \\ 0 & 0 & 1/\lambda_1 & 0 \\ 0 & 0 & 0 & 1/\lambda_2 \end{pmatrix}, \qquad \lambda_1, \lambda_2 > 0,\ \lambda_1 \ne \lambda_2,$$

so the image of the ball (D.25) is the ellipsoid

$$\frac{x_1^2}{\lambda_1} + \frac{x_2^2}{\lambda_2} + \lambda_1 p_1^2 + \lambda_2 p_2^2 \le R^2. \tag{D.29}$$

- *Conjugate slice.* Setting $x_2 = p_2 = 0$ (the x_1, p_1 plane) gives $\frac{1}{\lambda_1}x_1^2 + \lambda_1 p_1^2 \le R^2$: its area is $\pi R^2 \sqrt{\lambda_1}\sqrt{1/\lambda_1} = \pi R^2$, fully consistent with the symplectic-egg property.
- *Non-conjugate slice.* Intersecting (D.29) with the non-conjugate plane x_2, p_1 ($x_1 = p_2 = 0$) yields $\frac{1}{\lambda_1}x_1^2 + \lambda_2 p_2^2 \le R^2$, whose area is $\pi R^2 \sqrt{\frac{\lambda_1}{\lambda_2}} \ne \pi R^2$.
- *Symplectic assumption is essential.* Take $S' = \text{diag}(\lambda_1, \lambda_2, 1/\lambda_2, 1/\lambda_1)$; then $\det S' = 1$ but $S' \notin \text{Sp}(4, \mathbb{R})$. The slice in the x_2, p_2 plane now has area $\pi R^2 \sqrt{\lambda_1/\lambda_2} \ne \pi R^2$, confirming that only *symplectic* maps preserve the constant cross-sectional area in conjugate planes.

D.4 Canonical Transformations on Phase Space

General definition. A *canonical transformation* is a C^∞ diffeomorphism

$$f : \begin{pmatrix} x \\ p \end{pmatrix} \longmapsto \begin{pmatrix} x' \\ p' \end{pmatrix}, \qquad f^{-1} \in C^\infty. \tag{D.30}$$

whose Jacobian matrix

$$f'(x,p) = \frac{\partial(x',p')}{\partial(x,p)}. \tag{D.31}$$

is *symplectic* at every point (x, p); i.e.

$$f'(x,p)^T J\, f'(x,p) = J. \tag{D.32}$$

Linear canonical maps. Any symplectic matrix $S = \left(\begin{smallmatrix} A & B \\ C & D \end{smallmatrix}\right)$ induces the linear canonical transformation

$$\begin{pmatrix} x \\ p \end{pmatrix} \longmapsto S \begin{pmatrix} x \\ p \end{pmatrix}. \tag{D.33}$$

It is an invertible transformation, since symplectic matrices are invertible.

Translations and affine maps. Phase–space translations

$$\begin{pmatrix} x \\ p \end{pmatrix} \longmapsto \begin{pmatrix} x + x_0 \\ p + p_0 \end{pmatrix}. \tag{D.34}$$

have Jacobian Id_{2n}, trivially symplectic. Composing a linear canonical transformation with a translation yields the full class of *affine* canonical transformations.

Non-linear example ($n = 1$). Using polar–like variables (r, φ) in place of (x, p), define

$$(r,\varphi) \longmapsto \big(x,p\big) = \big(\sqrt{2r}\cos\varphi,\ \sqrt{2r}\sin\varphi\big), \qquad 0 \le \varphi < 2\pi. \tag{D.35}$$

Its Jacobian is

$$f'(r,\varphi) = \begin{pmatrix} \dfrac{1}{\sqrt{2r}}\cos\varphi & \dfrac{1}{\sqrt{2r}}\sin\varphi \\ -\sqrt{2r}\sin\varphi & \sqrt{2r}\cos\varphi \end{pmatrix}. \tag{D.36}$$

$$\det f'(r,\varphi) = 1. \tag{D.37}$$

so $f'(r, \varphi) \in \mathrm{Sp}(2, \mathbb{R})$ for every (r, φ): the map is canonical.

The construction extends to $n > 1$ by applying the same polar substitution to each conjugate pair (x_j, p_j).

D.5 Gromov's Theorem (1985)

D.5.1 Statement:

No canonical transformation can squeeze a phase–space ball B_R through a circular hole of radius $r < R$ cut in a conjugate plane $\Pi_j \equiv \{x_j, p_j\}$.

The "symplectic camel" metaphor. Why this nickname? Recall the scriptural saying:

> *Then Jesus said to his disciples, "Amen, I say to you, it will be hard for one who is rich to enter the kingdom of heaven. Again I say to you, it is easier for a camel to pass through the eye of a needle than for one who is rich to enter the kingdom of God."*

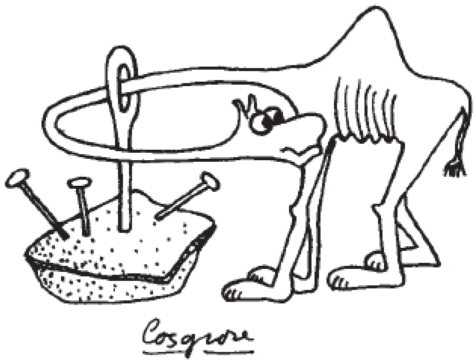

That is our symplectic camel— it cannot enter the eye of the needle!

D.5.2 The Symplectic Egg as a Linear Version of Gromov's Theorem

Picture the ball B_R as the "camel" and the hole of radius r in the plane $\Pi_j = \{x_j, p_j\}$ as the needle's eye. The symplectic-egg result is really just the linear (or affine) version of Gromov's non-squeezing statement.

Here's the idea: If we try to pass the egg $S(B_R)$ through that hole, its slice in Π_j must fit inside the circle of area πr^2. But the egg property says every such slice already has area πR^2. So for the squeeze to work we'd need $\pi R^2 \leq \pi r^2$, i.e. $R \leq r$. When $R > r$, the egg just won't go through. That's the linear case of Gromov's theorem because the symplectic egg is generated by a linear map S directly.

D.6 Dynamical Interpretation

Canonical transformations are fundamental in physics because Hamiltonian dynamics themselves are expressed as canonical transformations. Consider a particle of mass m moving along the x-axis under the influence of a scalar potential $V(x)$. The particle experiences a force:

$$F = -\frac{dV}{dx} = m\frac{dv}{dt} = \frac{dp}{dt}. \tag{D.38}$$

The equations of motion can thus be written:

$$\frac{dx}{dt} = \frac{p}{m}, \qquad \frac{dp}{dt} = -\frac{dV}{dx}. \tag{D.39}$$

D.6.1 Hamiltonian Formulation

Introducing the Hamiltonian function

$$H(x,p) = \frac{p^2}{2m} + V(x), \tag{D.40}$$

the previous equations are equivalent to Hamilton's equations:

$$\frac{dx}{dt} = \frac{\partial H}{\partial p}, \qquad \frac{dp}{dt} = -\frac{\partial H}{\partial x}. \tag{D.41}$$

This formulation naturally extends to n dimensions:

$$\frac{dx_j}{dt} = \frac{\partial H}{\partial p_j}, \qquad \frac{dp_j}{dt} = -\frac{\partial H}{\partial x_j}, \qquad 1 \leq j \leq n. \tag{D.42}$$

Hamiltonian Flows

More generally, the Hamiltonian H can depend on time or have a more complex form. In any case, solving Hamilton's equations determines a *flow* in phase space. If we denote the initial state by

$$\begin{pmatrix} x(0) \\ p(0) \end{pmatrix}, \tag{D.43}$$

then, assuming the solution exists and is unique at time t, the final state is given by

$$\begin{pmatrix} x(t) \\ p(t) \end{pmatrix} = \phi_t^H \begin{pmatrix} x(0) \\ p(0) \end{pmatrix}, \tag{D.44}$$

where ϕ_t^H is the Hamiltonian flow generated by H.

D.6.2 Trajectories and Liouville's Theorem

As time evolves, the initial point traces a curve in phase space, called a **flow curve** or **Hamiltonian trajectory**. A crucial point is that the flow ϕ_t^H is a *canonical transformation.* Thus Hamiltonian flows preserve phase-space volume, which is precisely the content of **Liouville's theorem**. The reason is simple: the Jacobian of a canonical transformation is a symplectic matrix S, hence $\det S = 1$.

Volume preservation alone is not unique to Hamiltonian dynamics—any map with $\det(\text{Jacobian}) = 1$ is volume-preserving. But because Hamiltonian flow is canonical, it is additionally constrained by *Gromov's theorem*; it is therefore more than just volume-preserving.

Conclusion: Liouville's theorem *and* Gromov's non-squeezing theorem both follow from the symplectic structure of phase space.

D.6.3 Comments on Gromov's Theorem

One reason this result was discovered so late is its apparent contradiction with classical intuition. At first sight, Gromov's theorem seems to contradict the usual reading of Liouville's theorem, which is probably why the "symplectic camel" remained unsuspected for so long.

Liouville's theorem guarantees *volume* preservation, but says nothing about *shape*. A Hamiltonian flow can stretch and fold a subset of phase space, potentially spreading it over vast regions while its projections onto certain planes shrink arbitrarily. This mechanism becomes even more pronounced as the number of degrees of freedom n increases.

Such observations raise deep philosophical questions. As Roger Penrose remarked (1989, p. 183), phase-space spreading

> *"suggests that classical mechanics cannot actually be true of our world."*

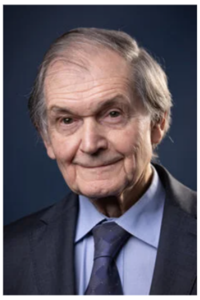

D.6.4 Shadows and Gromov's Theorem

Gromov's theorem implies that Hamiltonian evolution is much more structured than one might expect. To illustrate this, consider the phase-space ball B_R. Its orthogonal projection (or "shadow") onto any plane Π of conjugate coordinates x_j, p_j is a circle with area πR^2. If the ball evolves under a Hamiltonian flow ϕ_t^H, it may deform, but its volume remains constant. Yet, according to the symplectic camel principle, its shadow on Π_j will never shrink below πR^2.

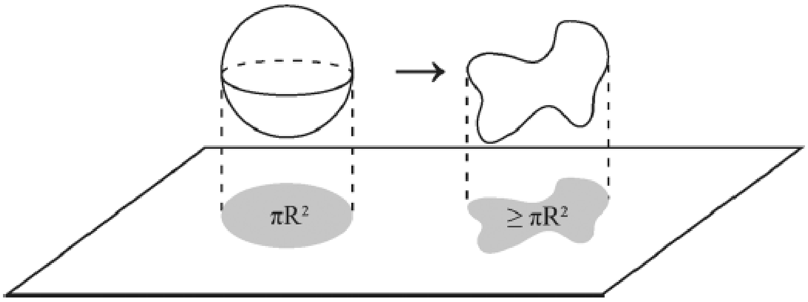

Figure D.1: Shadow of a deformed ball under Hamiltonian evolution.

In this bibliographic appendix, I have summarised the article [8].

Appendix E

Conservation of a Global Symmetry in a Nonlinear Flow

Theorem E.1 (Conservation of a Global Symmetry)**.** *Let $\rho(Z,t)$ be a particle density evolving in phase space $\mathbb{R}^{2n}$, according to a deterministic dynamic given by:*

$$\frac{dZ}{dt} = F(Z), \tag{E.1}$$

where $F : \mathbb{R}^{2n} \to \mathbb{R}^{2n}$ is a C^1 function admitting a differentiable flow $\Phi_t(Z)$, such that $\Phi_0(Z) = Z$ and

$$\frac{d}{dt}\Phi_t(Z) = F(\Phi_t(Z)). \tag{E.2}$$

Assume the density evolves according to:

$$\rho(Z,t) = \rho_0(\Phi_{-t}(Z)), \tag{E.3}$$

where ρ_0 is the initial phase-space density.

Let $S : \mathbb{R}^{2n} \to \mathbb{R}^{2n}$ be a differentiable transformation such that:

- *(Initial symmetry) $\rho_0(SZ) = \rho_0(Z)$ for all $Z \in \mathbb{R}^{2n}$,*
- *(Flow invariance) $\Phi_t(SZ) = S\Phi_t(Z)$ for all $t \in \mathbb{R}$, $Z \in \mathbb{R}^{2n}$.*

Then, for all $t \in \mathbb{R}$ and all $Z \in \mathbb{R}^{2n}$, we have:

$$\rho(SZ,t) = \rho(Z,t). \tag{E.4}$$

Proof. By the definition of the time-evolved density:

$$\rho(SZ,t) = \rho_0(\Phi_{-t}(SZ)). \tag{E.5}$$

Using the flow invariance hypothesis:

$$\Phi_{-t}(SZ) = S\Phi_{-t}(Z). \tag{E.6}$$

Then, by the initial symmetry:

$$\rho_0(S\Phi_{-t}(Z)) = \rho_0(\Phi_{-t}(Z)) = \rho(Z,t). \tag{E.7}$$

Therefore, $\rho(SZ,t) = \rho(Z,t)$, which completes the proof. ☐

Bibliography

[1] V. V. Nesvizhevsky, H. G. Börner, A. K. Petukhov, H. Abele, S. Baeßler, F. J. Rueß, T. Stöferle, A. Westphal, A. M. Gagarski, G. A. Petrov, and A. V. Strelkov, “Quantum states of neutrons in the earth’s gravitational field”, Nature **415**, 297–299 (2002) 10.1038/415297a.

[2] T. Killian et al., “Grasian: towards the first demonstration of gravitational quantum states of atoms with a cryogenic hydrogen beam”, arXiv preprint arXiv:2301.12731 (2023).

[3] J. J. Sakurai and J. Napolitano, *Modern quantum mechanics*, 2nd ed. (Cambridge University Press, Cambridge, 2017).

[4] P. Yzombard, *Logiqs — project notice*, 2023.

[5] P. Jansen and F. Merkt, “Manipulating beams of paramagnetic atoms and molecules using inhomogeneous magnetic fields”, Progress in Nuclear Magnetic Resonance Spectroscopy **120–121**, 118–148 (2020) 10.1016/j.pnmrs.2020.08.002.

[6] J. R. Taylor, *Classical mechanics* (University Science Books, 2005) Chap. 13.

[7] H. Qin, *Advanced fuel fusion, phase space engineering, and structure-preserving geometric algorithms*, arXiv:2402.09622v1, 2024, arXiv:2402.09622 [physics.plasm-ph].

[8] M. A. de Gosson, “The symplectic egg in classical and quantum mechanics”, American Journal of Physics **81**, 328–335 (2013) 10.1119/1.4791775.

[9] T. Bergeman, G. Erez, and H. J. Metcalf, “Magnetostatic trapping fields for neutral atoms”, Phys. Rev. A **35**, 1535–1546 (1987) 10.1103/PhysRevA.35.1535.

[10] I. Stewart, “The symplectic camel”, Nature **329**, 17–18 (1987) 10.1038/329017a0.